AIAA 2000-0531
Receptivity of Hypersonic Boundary Layers to Freestream Disturbances

Xiaolin Zhong
University of California, Los Angeles
Los Angeles, CA

38th Aerospace Sciences Meeting & Exhibit
10-13 January 2000 / Reno, NV

RECEPTIVITY OF HYPERSONIC BOUNDARY LAYERS TO FREESTREAM DISTURBANCES

Xiaolin Zhong *
University of California, Los Angeles, California 90095

ABSTRACT

The receptivity of hypersonic boundary layers to freestream disturbances, which is the process of environmental disturbances initially entering the boundary layers and generating the growth of instability waves, is altered considerably by the presence of the bow shocks in the flow fields. In a previous paper (AIAA paper 97-0756), we have presented some initial results on numerical simulations of the receptivity of a hypersonic boundary layer to freestream monochromatic planar acoustic disturbances for a Mach 15 flow over a parabolic leading edge. The initial results showed that the instability waves developed in the hypersonic boundary layer behind the bow shock contain both the first and second mode instabilities. The purpose of this paper is to present the results of our subsequent parametric study through a large number of computational simulations with different parameters. The effects of nature of freestream waves, Reynolds number, nose bluntness, and wall temperatures on the leading edge receptivity are investigated.

1 INTRODUCTION

The prediction of laminar-turbulent transition in hypersonic boundary layers is a critical part of aerodynamic design and control of hypersonic vehicles [1,2]. In general, the transition process in boundary layers is the result of nonlinear response of the laminar boundary layers to forcing disturbances [3-6]. The forcing disturbances can originate from many difference sources including freestream disturbances, surface roughness and vibrations, etc [7]. In an environment with small initial disturbances, the paths to transition consist of three stages: 1) receptivity, 2) linear eigenmode growth or transient growth, and 3) nonlinear breakdown to turbulence. Among them, the receptivity mechanism provides important initial conditions of amplitude, frequency, and phase for the instability waves in the boundary layers [8-10]. For hypersonic boundary-layer flow over blunt bodies, the receptivity process is much more complex and is currently not well understood [11,12]. Figure 1 shows a schematic of wave field interactions near the hypersonic leading edge affected by freestream disturbances. The receptivity phenomena are altered considerably by the bow shock in front of the body. The interaction of the waves with the shock can affect the transition of the hypersonic boundary layer behind the shock.

In [13], we developed and validated a set of fifth-order shock fitting numerical methods for the DNS of the receptivity of hypersonic boundary layers over blunt bodies. Both the unsteady bow shocks and the development of instability waves in the boundary layers are simultaneously included in the simulations. Subsequently, we [14] investigated the receptivity of a hypersonic boundary layer to 2-D freestream monochromatic planar acoustic disturbances by DNS for a Mach 15 flow over a parabolic leading edge. The initial results showed that the instability waves developed in the hypersonic boundary layer behind the bow shock contain both the first and second mode instabilities. In order to gain a deeper understanding of the the leading edge receptivity process of hypersonic flows over blunt nose, parametric studies are necessary to study the effects on receptivity by nose radius, wall cooling, Reynolds numbers, and other freestream disturbances.

The purpose of the present studies is to conduct parametric studies by means of numerical simulations for a large number of computational cases with different parameters. These results demonstrate in depth the properties of the hypersonic receptivity process. To focus our attention on the leading edge receptivity only, we limit our parametric studies to the two-dimensional instability waves in hypersonic boundary layers induced by 2-D free stream disturbances. The generation of boundary-layer waves in the boundary layer are studied based on the direct numerical simulations (DNS). The numerical solutions of the full Navier-Stokes equations are compared with theoretical analysis, such as the local normal-mode linear stability analysis. The numerical accuracy of the DNS results for such hypersonic boundary layer receptivity have been evaluated by grid refinement studies and by comparison with available experimental or theoretical results. The detailed results of code validation and error assessments are not presented here. They have been reported in several previous papers Ref. [13,15].

*Associate Professor, Mechanical and Aerospace Engineering Department, e-mail: xiaolin@seas.ucla.edu, Senior Member AIAA.

2 GOVERNING EQUATIONS

The governing equations are briefly presented in this section, followed by a brief discussion of the numerical methods and accuracy in Section 3. Details of the governing equations and gas models, as well as a review of the hypersonic receptivity, stability, and transition have been presented in [13].

The governing equations for the direct numerical simulations of hypersonic flows over a blunt wedge are the unsteady three-dimensional Navier-Stokes equations in the following standard conservation-law form:

$$\frac{\partial U^*}{\partial t^*} + \frac{\partial F^*{}_j}{\partial x_j^*} + \frac{\partial F^*{}_{vj}}{\partial x_j^*} = 0 \qquad (1)$$

where superscript "*" represents dimensional variables, and t^* and x_j^* are components of Cartesian coordinates and time respectively.

In the present study, the gas is assumed to be a thermally and calorically perfect gas. The viscosity coefficient is calculated according to the Sutherland law with the assumption of zero bulk viscosity. It is also assumed that the gas has a constant ratio of specific heats and a constant Prandtl number. The thickness of the bow shock is assumed to be thin so that it is treated as a mathematically discontinuous surface satisfying the the Rankine-Hugoniot relations. These assumptions are a significant simplification of actual hypersonic flows, where the equilibrium and nonequilibrium real-gas effects may be significant and the bow-shock thickness may not be very thin. However, these simple models are necessary in order to study the main features of the stability and receptivity of viscous hypersonic flows.

In receptivity simulations, the flow variables at the supersonic free stream in front of the bow shock are fixed for a steady flow, and are a steady flow field plus a weak acoustic wave field for unsteady flows. The body surface is assumed to be a non-slip wall with a given constant wall temperature T_w^*. The bow shock is assumed to be an infinitely thin moving surface, where flow variables across the shock are governed by the Rankine-Hugoniot conditions. The Rankine-Hugoniot relations lead to jump conditions for flow variables behind the shock as functions of freestream flow variables at the shock and the local shock normal velocity v_n. In order to compute the flow variable behind the shock, the velocity of the shock front v_n is needed. The shock normal velocity is determined by a characteristic compatibility equation immediately behind the shock.

Because the flow field behind the bow shock is not uniform, the flow variables are nondimensionalized using the freestream conditions as characteristic variables. Specifically, we nondimensionalize the velocities with respect to the freestream velocity U_∞^*, length scales with respect to a reference length d^*, density with respect to ρ_∞^*, pressure with respect to p_∞^*, temperature with respect to T_∞^*, time with respect to d^*/U_∞^*, vorticity with respect to U_∞^*/d^*, entropy with respect to c_p^*, wave number by $1/d^*$, etc. The dimensionless flow variables are denoted by the same dimensional notation but without the superscript "*".

3 RECEPTIVITY SIMULATIONS

The receptivity of a two-dimensional boundary layer to weak freestream acoustic disturbance waves for hypersonic flows past a parabolic leading edge at zero angle of attack are considered. The body surface is a parabola given by

$$x^* = b^* y^{*2} - d^* \qquad (2)$$

where b^* a given constant and d^* is taken as the refcrence length. The nose radius of curvature is $r^* = 1/(2b^*)$.

The receptivity problems consider freestream disturbances superimposed on the steady mean flow to investigate the development of boundary-layer waves under the influence of bow shock interaction. The freestream disturbances are assumed to be weak monochromatic planar fast acoustic or entropy waves with wave fronts normal to the center line of the body. The wave fields of the unsteady viscous flows are represented by the perturbations of instantaneous flow variables with respect to their local steady based flow variables. The flow variable perturbed by the freestream acoustic wave before reaching the bow shock can be written in the following form:

$$q' \quad = \quad |q'|\, e^{ik(x-ct)} \qquad (3)$$

where q represents the perturbation of any flow variables. For acoustic or entropy waves in the freestream, the perturbation amplitudes of nondimensional flow variables satisfy the following relations:

Acoustic Waves:

$$|s'|_\infty = |v'|_\infty = 0$$
$$|\rho'|_\infty = |p'|_\infty/\gamma = |u'|_\infty M_\infty = \epsilon M_\infty$$

Entropy Waves:

$$|u'|_\infty = |v'|_\infty = |p'|_\infty = 0$$
$$|\rho'|_\infty = -|s'|_\infty = \epsilon M_\infty$$

where ϵ is a small number representing the relative amplitudes of the freestream waves.

The nondimensional wave speeds are $c = 1 + M_\infty^{-1}$ for fast acoustic waves and $c = 1$ for entropy waves. The parameter k is the dimensionless freestream wave number which is related to the dimensionless circular frequency ω by:

$$\omega = k\, c \qquad (4)$$

A Reynolds number of the flow is defined as

$$Re_\infty \quad = \quad \frac{\rho_\infty^* U_\infty^* d^*}{\mu_\infty^*} \qquad (5)$$

The forcing frequency of the freestream acoustic wave is represented by either a dimensionless frequency F defined by

$$F = 10^6 \frac{\omega^* \nu^*}{U_\infty^{*2}} = 10^6 \, \omega / Re_\infty \, . \tag{6}$$

or represented by a Strouhal number S defined by

$$S = \frac{\omega^* d^*}{U_\infty^*} \tag{7}$$

The Strouhal number S represents the relative bluntness of a blunt leading edge if the nose radius of curvature is used for d^*, and F represents the wave frequency with respect to viscous flow scales. For the same forcing frequency ω, the wave numbers for the fast acoustic waves (k_a) and entropy waves (k_e) in the freestream are related to each other by the following relations:

$$k_\mathrm{e} = k_\mathrm{a} \frac{M_\infty + 1}{M_\infty} \tag{8}$$

In this paper, the receptivity problems are studied numerically by solving the unsteady Navier-Stokes equations using a fifth-order shock fitting scheme described in [13,15]. The numerical accuracy of the solutions are also evaluate by grid refinement studies for both the steady and unsteady solutions. The numerical simulation for an unsteady hypersonic layer receptivity problem is carried out in three steps. First, a steady flow field is computed by advancing the unsteady flow solutions to convergence with no disturbances imposed in the freestream. Second, unsteady viscous flows are computed by imposing a continuous planar acoustic or entropy single-frequency disturbance wave on the steady flow variables at the freestream side of the bow shock. The unsteady calculations are carried out for about 20 to 40 periods in time until the solutions reach a periodic state in time. Third, the unsteady computations are carried out for one additional period in time to perform a FFT on the perturbation field to obtain the Fourier amplitude and phase of the perturbations of the unsteady flow variables throughout the flow field.

4 FLOW CONDITIONS

A number of computational cases have been considered to study parametric effects of frequency, nose bluntness, freestream wave types, wall cooling, and Reynolds numbers on hypersonic receptivity. All cases presented in this paper have the following common flow conditions:

$M_\infty = 15$ $\quad T_\infty^* = 192.989\, K$
$p_\infty^* = 10.3\, Pa$ $\quad \gamma = 1.4$
$Pr = 0.72$

The computational cases are classified into four groups (A – D) as follows:

A. Freestream Acoustic Waves:
$Re_\infty = 6026.6$ $\quad T_w^* = 1000K$
$r^* = 0.0125\, m$ $\quad d^* = 0.1\, m$
$\epsilon = 5 \times 10^{-4}$ to 10^{-1}

Seven Cases of Frequencies:

Case Number	k_∞	F	S
A.1	15	2655	2.00
A.2	12.5	2212.5	1.67
A.3	10	1770	1.33
A.4	7.5	1327.5	1.00
A.5	5.7	1008.9	0.76
A.6	4.35	769.95	0.58
A.7	3	531	0.40

B. Freestream Entropy Waves:
All conditions same as Case A except freestream entropy waves

Eight Sub-Cases of Frequencies:

Case Number	k_∞	F	S
B.1	16	2655	2.00
B.2	15	2489.1	1.88
B.3	12.5	2074.2	1.56
B.4	10	1659.4	1.25
B.5	7.5	1244.5	0.94
B.6	5.7	945.84	0.71
B.7	4.6	763.31	0.58
B.8	3.5	580.78	0.44

C. Wall Temperature Effects:
All conditions same as Case A except $T_w^* = 2000K$

Six Cases of Frequencies:

Case Number	k_∞	F	S
C.1	15	2655	2.00
C.2	12.5	2212.5	1.67
C.3	10	1770	1.33
C.4	7.5	1327.5	1.00
C.5	5.7	1008.9	0.76
C.6	4.5	796.5	0.6

D. Reynolds Number Effects:
All conditions same as Case A except r^*, d^*, Re_∞ are 10 times as large
$Re_\infty = 60266$

Six Cases of Frequencies:

Case Number	k_∞	F	S
D.1	18.25	323.0	2.43
D.2	15	265.5	2.00
D.3	12.5	221.3	1.67
D.4	9.487	167.9	1.26
D.5	7.5	132.8	1.00
D.6	5.7	100.9	0.76

5 STEADY FLOW SOLUTIONS

The general features of steady flow solutions have been presented in [16]. In this section, we discuss the steady flow characteristics for the viscous hypersonic flow over parabolas relevant to the receptivity studies.

5.1 Vorticity Interaction

Hypersonic flow fields over a blunt leading edge consists of three main regions as shown in Fig. 2. Region I is the rotational inviscid outer field, where vorticity is generated by the curved bow shock according to the Crocco's theorem. Region II is the viscous stagnation flow region, where the boundary layer thickness is constant for incompressible flow and is near constant for compressible flows. Region III is the boundary layer flow downstream where boundary layer thickness grows along the streamwise directions. There is an interaction between region I and region III due to non-zero vorticity outside the boundary layer created by the bow shock. Such vorticity interaction, which may play an important role in the stability of hypersonic boundary layer downstream, is studied in this paper through the numerical solutions of the full Navier-Stokes equations.

The inviscid vorticity field immediately behind the bow shock can be analyzed by making the inviscid flow assumption for flow near the shock. The inviscid vorticity jump across the bow shock was derived by Truesdell [17], Lighthill [18], and by Hayes [19] using the Rankine-Hugoniot relation and Crocco's theorem or momentum equation in the direction normal to the shock. For a bow shock in a uniform freestream flow, the vorticity vector behind the shock depends only on the density ratio across the shock and the shock curvature tensor, i.e.,

$$\omega_{\rm shk} = u_t \; k \; \frac{(1-\rho_\infty/\rho_s)^2}{\rho_\infty/\rho_s} \qquad (9)$$

where k is the curvature of the shock and u_t is the local tangential velocity component.

Fig. 3 compares the local vorticity components immediately behind the bow shock for the steady Navier-Stokes solutions of Case A and the inviscid theoretical results determined by Eq. (9). The two sets of results agree very well. There are slight differences at the valley of vorticity distribution because the viscous effects are not accounted for in Eq. (9). In the figure, the negative sign in the vorticity represents that the vorticity is pointing in the negative z direction. The magnitude of the vorticity generated by the bow shock reach a maximum near the leading edge and decreases afterward.

The bow shock generates curved streamlines behind it as shown in Fig. 4. The ratio of the local streamline curvature at the shock to the shock curvature at the same point was derived by Hornung as a function of local shock angle, Mach number and γ only, i.e. [20],

$$\frac{k_{\rm streamline}}{k_{\rm shk}} = f(\beta, M_\infty, \gamma) \qquad (10)$$

Figure 5 compares streamline to shock curvature ratios between numerical solutions of the Navier-Stokes equations and the theoretical results. The two sets of results compare very well with each other. The curvature ratio is zero at the stagnation line ($\beta = 90°$) because the streamline curvature is zero. The ratio is negative near the stagnation point because the streamlines are concave there. It then passes through the zero curvature point and become positive as β decreases.

The vorticity generated behind the shock is convected downstream in region I, where the flow is isentropic along a streamline in steady inviscid flows. For steady inviscid flow with a uniform freestream, it can be shown [21] that

$$\frac{D}{Dt}\left(\frac{\boldsymbol{\omega}}{T\rho}\right) = \frac{1}{\rho}\,\boldsymbol{\omega}\cdot\nabla\left(\frac{\boldsymbol{u}}{T}\right) \qquad (11)$$

Equation (11) leads to the result that the ratio of vorticity to pressure ω/p is constant along streamlines for steady 2-D perfect-gas flow. Since hypersonic flow over a parabola has favorable pressure gradients in region I, the magnitude of vorticity drops along a streamline for inviscid flows. The vorticity created by the bow shock interacts with the boundary layer when the streamlines enter the boundary layer downstream. Figure 6 shows steady vorticity solutions along the body surface and behind the bow shock. The vorticity along body surface is generated by viscosity due to shear effects in the boundary layer. The vorticity interaction can be characterized by the ratio of maximum vorticity in magnitudes behind the shock and on the body surface. For the present case A, the ratio is

$$\frac{\max(\omega_{\rm shk})}{\max(\omega_{\rm wall})} = 0.0465 \qquad (12)$$

which indicates a weak vorticity interaction between region I and III. According to Eq. (9), the vorticity behind the shock becomes stronger when the density ratio

across the shock decreases. Therefore, it is expected that the vorticity interaction will be stronger when the density ratio across the shock is very small, which is the case for hypersonic flows with real gas effects.

5.2 Solutions in the Boundary Layer Region

The numerical solutions of the full Navier-Stokes equations are compared with boundary layer equations results. An approximate locally similar boundary layer solution is calculated by using a similarity transformation [22], i.e.,

$$\xi^* = \int_0^{s^*} \rho_e^* u_e^* \mu_e^* \, ds^* \tag{13}$$

$$\eta = \frac{u_e^*}{\sqrt{2\xi^*}} \int_0^{n^*} \rho_e^* \, dn^* \tag{14}$$

where, s^* and n^* are the local dimensional natural coordinates defined by the surface length and distance along the wall-normal direction, respectively. The variable η is the similarity boundary layer nondimensional coordinates.

The parameters ρ_e^*, u_e^*, and μ_e^* are dimensional density, tangential velocity, and viscosity coefficients for inviscid flow on the wall, and they are taken to be the freestream boundary conditions for the boundary layer equations. For hypersonic flow over a parabola, the determination of boundary edge conditions can be obtained from inviscid solutions by computing the Euler equations. Since the pressure does not change much across the boundary layers, we use the surface pressure obtained by the Navier-Stokes equations as the edge inviscid pressure p_e for the boundary layer calculations. The other inviscid conditions, ρ_e^*, u_e^*, and μ_e^* are on the surface, and are obtained by an isentropic relation by assuming they are corresponding to the inviscid stagnation streamline behind the normal part of the bow shock.

The boundary layer solutions in region II and III are obtained by using an approximate local similarity solution by assuming

$$\frac{u^*}{u_e^*} = f(\eta) \quad \text{and} \quad \frac{T^*}{T_e^*} = g(\eta) \tag{15}$$

Substituting Eqs. (15) into the compressible boundary layer equations, and neglecting the effects of body surface curvature, leads to the following standard similarity equations,

$$(Cf'')' + ff'' + \alpha(g - f'^2) = 0 \tag{16}$$

$$(\frac{C}{Pr}g')' + fg' + (\gamma - 1)M_e^2 C f''^2 = 0 \tag{17}$$

where $C = \frac{\rho^*\mu^*}{\rho_e^*\mu_e^*}$ is the Chapman-Rubesin parameter, M_e is the edge Mach number, Pr is the Prandtl number, and $\alpha = \frac{2\xi^*}{u_e^*}\frac{du_e^*}{d\xi^*}$ is the edge velocity gradient parameter. This nonlinear set of ordinary differential equations with appropriate boundary conditions are solved by a shooting method based on a fourth-order Runge-Kutta scheme.

Figure 7 shows the distribution of the Navier-Stokes solutions along the body surface for skin friction coefficients and heat transfer coefficients nondimensionalized by freestream parameters. The characteristics of the solutions in Viscous region II and III is shown in the figure. In the leading edge region, shear stress coefficient C_f has a rapid and almost linear increase, which represents the stagnation region II boundary layer solution. As x increases, the C_f reaches a peak and decreases as x increases further down stream, which is a typical boundary layer solution in favorable pressure gradients in region III.

The Navier-Stokes solutions and independently obtained boundary-layer similarity solutions for the same flow conditions are compared by normalizing the Navier-Stokes solutions by local boundary-layer edge parameters. Figure 8 shows a local shear stress coefficient c_f and Stanton number st defined by local boundary layer variables, i.e.,

$$c_f = \frac{\tau_w^*}{\rho_e^* u_e^{*2}/2} \sqrt{\frac{2\xi^*}{\mu_e^{*2}}} \tag{18}$$

$$st = \frac{q_w^*}{\rho_e^* u_e^* (h_{0e}^* - h_w^*)} \sqrt{\frac{2\xi^*}{\mu_e^{*2}}} \tag{19}$$

The figure shows that the current Navier-Stokes solutions agree very well with the boundary-layer results for both skin friction and heat transfer rates. The results also show that there is also a similar characteristic in the c_f and st as the Reynolds analogy in flat plate boundary layers in that $c_f/(2st)$ is close to a constant. The ratio is near 1.14 for the current flow conditions.

The interaction of solutions in region I and III can be shown by plots of tangential velocity u^*/u_e^* vs. boundary layer coordinates η along wall-normal grid lines. Figure 9 compares the velocity profiles from the boundary layer solutions with those from the Navier-Stokes solutions for two cases of different Reynolds numbers (Cases A and D), where $i = 12$ is an index near the nose region while $i = 127$ is located further downstream. The x coordinates of the intersecting points of grid lines and the body surface for Case A are:

Table 1. x coordinates for surface grid points.

Index i	x_s Coordinates
50	-0.756873
70	-0.557069
90	-0.297524
110	0.0376505
130	0.465454
150	1.00326

The results show a very good agreement in the boundary layer up to the edge of the boundary layer located

approximately at $\eta = 3$ for this case as shown in Fig. 10. The velocity profiles are nearly independent of the Reynolds number when they are normalized by local boundary layer similarity parameters. The velocity profile has an inflection point near the leading edge due to strong inviscid vorticity outside the boundary layer. As the flow moves downstream, the velocity profiles become fuller and approach the boundary layer solutions. The figure also shows that the boundary thickness is located at approximately $\eta = 3$, which is nearly constant at various grid stations along the body surface.

The viscous flow in region II of the stagnation point can also be solved by the boundary layer equations governed by Eqs. (16) and (17) with $\alpha = 1$. The results are compared with the Navier-Stokes solution at the stagnation point for Case D of $Re_\infty = 60266$. Fay and Riddell [23] did extensive stagnation line boundary layer calculations on stagnation heating rates. Fay and Riddell's result for the stagnation point heating coefficient h defined in the experimental studies are:

$$q_w = 0.570\ Pr^{-0.6}\ c_p\ \sqrt{\rho_e \mu_e K}\ \left(\frac{\rho_w \mu_w}{\rho_e \mu_e}\right)^{0.1} (T_e - T_w) \quad (20)$$

where K is the streamwise velocity gradient obtained approximately by the Newtonian theory for hypersonic flow at the stagnation point:

$$K = \frac{du_e}{ds} = \frac{1}{R}\sqrt{\frac{2(p_e - p_\infty)}{\rho_e}} \quad (21)$$

The Navier-Stokes solutions of stagnation heating rate is compared with the theoretical results by using a nondimensional parameter

$$\frac{Nu}{\sqrt{Re_x}} = \frac{q_w Pr}{\sqrt{\rho_e \mu_e K}(h_e - h_w)} \quad (22)$$

For Case D of Mach 15 flow and $Re_\infty = 60266$, the Navier-Stokes solutions, the Boundary layer computations, and the curve fit of Fay and Riddell given by Eq. (20) are compared for the heating parameter $\frac{Nu}{\sqrt{Re_x}}$. The values are 0.5063, 0.5383, 0.5523, respectively. The Navier-Stokes solutions agree reasonably well with the boundary layer prediction. The difference between the results are consistent with the uncertainty in computing the value of K.

6 UNSTEADY FLOW SOLUTIONS

In this section, the receptivity of boundary-layer instability waves to planar acoustic and entropy disturbances in the freestream is studied for two-dimensional hypersonic flow over a parabolic leading edge. The unsteady flow solutions are obtained by imposing acoustic or entropy disturbances to the basic flow in the freestream. The flow conditions of four groups of computational cases are tabulated in Section 4.

6.1 Case A: Freestream Acoustic Waves

The first group of cases are the receptivity simulations for freestream planar acoustic waves. Forcing frequency F is in the range of 531 to 2655. Some initial results of the acoustic receptivity have been presented in [16]. The results of parametric studies are presented here.

Figure 11 shows the contours for the instantaneous perturbation u' and the velocity vectors after the flow field reaches a time periodic state for Case A.1. The instantaneous contours show interaction of the freestream disturbances with the bow shock and the development of instability waves in the boundary layer on the surface. Figure 12 shows the distribution of instantaneous velocity perturbations due to the wave field development in the boundary layer along the $j = 30$ grid line near the body surface. There are two distinct sections of different wave patterns in the boundary layers, one is developed from the leading edge at $x < 0.2$ and the other is developed further downstream at $x > 0.2$. The peak oscillations for the wave in the first region are very close to the wall surface and there is mainly one peak in the oscillation magnitudes across the boundary layer. The second region develops oscillations away from the wall with two magnitude peaks. Figure 11 also shows that the first region shows very strong vortical wave patterns, while the second region shows relatively weak vortical waves. These two sections were identified in [16] as first and second mode regions respectively.

On the other hand, the change of wave modes does not exist in region I which is outside of the boundary layer as shown in Fig. 13, which shows the distribution of instantaneous perturbation of u' immediately behind the shock. There is only a single wave pattern in the solution behind the bow shock.

Temporal Fourier analysis is carried out on local perturbations of unsteady flow variables after a time periodic state has been reached. The Fourier transform for the real disturbance functions lead to:

$$q'(x,y,t) = \Re\{\sum_{n=0}^{N} |q_n(x,y)|\ e^{i\,[-n\omega t + \phi_n(x,y)]}\} \quad (23)$$

where ω is the forcing frequency, $q'(x,y,t)$ represents any perturbation variables, and $|q_n(x,y)|$ and $\phi_n(x,y)$ are real variables representing the local perturbation amplitude and phase angle respectively. The subscript n represents the wave modes of the perturbation fields, where $n = 0$ is the mean flow distortion, $n = 1$ is the fundamental mode, and $n = 2$ is the second harmonic, etc. These variables indicate the amplitude of local disturbances and the local phase angle with respect to the forcing waves in the freestream. The averaged kinetic energy per unit volume and Reynolds stress can also be computed using the following formulas:

$$k = \frac{1}{2}\overline{\rho\,(u'^2 + v'^2)} = \frac{\rho}{2}\sum_{n=0}^{N}(|u_n|^2 + |v_n|^2) \quad (24)$$

$$\tau_{12} = -\overline{\rho\, u'\, v'} = -\rho \sum_{n=0}^{N} [|u_n|\ |v_n|\ \cos(\phi_{un} - \phi_{vn})] \tag{25}$$

For perturbations in the boundary layer near the body surface, we can define a local growth rate α_r and a local wave number α_i of the perturbation fields by,

$$\alpha_i = \frac{1}{|q_1|}\frac{d|q_1|}{dx} \tag{26}$$

$$\alpha_r = \frac{d\phi_1}{dx} \tag{27}$$

where the derivatives are taken along a grid line parallel to the body surface.

Figure 14 shows the contours of Fourier amplitudes and phase angles for the horizontal velocity components for the case of $F = 2655$. There is a strong growth near the leading edge in the boundary layer near the wall, followed by a rapid decay and transition to another wave mode. This can be shown in Fig. 15 for the amplitude distribution of the velocity perturbations near the parabola surface. These figures show two distinct main regions of instability waves. The figure also shows that the first mode is much stronger than the second mode for the test case at this particular frequency.

The propagation of the perturbation waves are represented by the spatial distribution of lines of constant phase angles shown in Fig. 14. Notice that some of the discontinuous contour lines in the phase angles with jumps in phase angle of multiples of 360° are not real discontinuities. The decay of first mode and the growth of the second mode is shown by a sudden phase change near the body surface around $x = 0.2$. The phase structure has one more variation across the boundary layer after the change of modes.

Local parallel linear stability theory (LST) is used to identify the boundary layer eigenmodes and to analyze the instability mechanism and the bow-shock effects. The LST is used to obtain instability modes based on the numerically obtained basic flow between the body and the bow shock. The LST code is a spatial stability code developed by Hu and Zhong [24] based on both a fourth-order finite difference global method and a spectral global method. In LST analysis, the disturbance equations are reduced to an eigenvalue problem by assuming the perturbations of flow variables in a normal mode form:

$$q' = \hat{q}(y_n)\, e^{i(-\omega t + \alpha s)} \tag{28}$$

where n and s is coordinate along the wall-normal and surface directions, α is the wave number, and $\hat{q}(y_n)$ is the eigenfunction. In the LST analysis, α and $\hat{q}(y_n)$ are obtained as the eigenvalue and eigenfunction of the stability equations for a given forcing frequency ω. For the spatial problem, ω is real, and α is a complex wave number,

$$\alpha = \alpha_r + i\ \alpha_i \tag{29}$$

where α_r and α_i represent the spatial wave number and growth rate of a wave mode respectively. The wave is unstable when α_i is negative.

In this paper, the wave modes obtained by the LST analysis are compared with the Fourier amplitude and wave number/growth rates defined by Eqs. (26) and (27). Because the eigenfunction represents only the homogeneous transient solution in the receptivity process, the comparison is used mainly for the purpose of identification of the wave modes obtained by the receptivity simulations. Since the simulation is an initial boundary value problem with non-homogeneous forcing terms in the freestream, while LST involves a homogeneous normal mode problem, it is expected the two solutions will not agree in region I located outside of the boundary layer.

Figure 16 shows the local wave number α_r in the boundary layer along a grid line near the parabola surface for the case of $F = 2655$. The numerical solutions include the wave number computed using both temperature and entropy perturbations. The LST results of the first, second and third modes are compared with the results obtained by numerical simulations. In the first mode region, the wave number increases (wavelength decreases) along the x direction. The figure shows that the LST first mode wave number has the closest agreement with the numerical wave solutions in this region. The results agree reasonably well considering the fact that LST is based on a parallel flow assumption, while the numerical solution is obtained in a flow field which is not strictly parallel and with the effects of surface curvature. As the waves develop downstream, the wave mode in the simulations undergo a gradual transition from the first mode to the second and third modes further downstream. Therefore, the results indicate that the instability waves excited in the first region are dominated by the first mode, followed by a gradual transition to the second and third modes.

The identification of the wave modes induced by freestream disturbances is further examined by comparing the LST eigenfunctions with Fourier amplitudes of the Navier-Stokes solutions. For the purpose of comparison, the eigenfunctions are normalized by their respective peak values near the wall. Figure 17 shows such comparison for the temperature amplitudes along grid lines normal to parabola surface at several i grid stations for the case of $F = 2655$. The figure shows that numerical solutions at earlier stations of $i = 50$ and 80 agree closer to the LST first mode in the region inside of the boundary layer. At later stations, the DNS results gradually change to profiles that are closer to the LST 2nd mode at $i = 100$ and 120, the LST 3rd mode at $i = 140$ and 160. The figure also shows that due to the effects of interaction of the bow shock with the flow dis-

turbances, the DNS produce very complex flow distributions in the inviscid region I. The variations outside the boundary layers are those induced by the forcing disturbances and their interaction with the bow shock. The DNS results and LST ones agree mainly inside the boundary layer in the wall region. In the flow region outside the boundary layer, the two solutions do not agree because the DNS solutions contain both the wave modes and the nonhomogeneous solutions induced by the forcing wave in the freestream.

It is found that the agreement between the LST first and second mode eigenfunctions and DNS results becomes better for test cases of lower frequencies. Figure 18 compares the LST first-mode eigenfunction with amplitudes of the simulation along a wall-normal direction at $x = 0.5521$ for the case of $F = 1770$. The DNS results agree very well with LST results inside the boundary layer. Again, the disagreement outside the boundary layer near the bow shock is expected because the effects of the forcing disturbances are not considered in the linear stability analysis.

For hypersonic flows over a blunt body, any freestream wave interaction with the shock always generates a combination of all three kinds of waves: acoustic, entropy, and vorticity waves. In a previous paper, Zhong et al. [16] showed that the inviscid entropy and vorticity waves based on the Euler equations are singular at the stagnation point. Such a singularity creates a wide range of length scales for these waves near the leading edge region. The singularity is removed in the viscous flow solutions.

Figures 19 and 20 show the variation of local pressure and entropy perturbation amplitudes along the stagnation line. The pressure disturbances show a typical acoustics interaction with a solid wall. The variation in pressure amplitudes is the result of the back and forth propagation and reflection of the acoustic wave. The existence of the boundary layer on the wall does not have a strong effect on the pressure waves propagation in the flow fields and the reflection from the wall. On the other hand, the entropy distribution shows a sharp change in entropy amplitudes in a region very close to the wall. There are two wave patterns along the stagnation line. The propagation in the region of $x < -1.02$ is a normal entropy wave propagation with slight damping on the wave because of viscosity. This region corresponds to the region outside of the boundary layer in the mean flow. The second region at $x > -1.02$ is the region inside the boundary layer induced by the incoming entropy waves. The wave is first amplified near the wall, but then decreases in a region very close to the wall. The thickness of the small region has a length scale much smaller than the lengthscale of the boundary layer. Such features of entropy perturbations exist for all cases considered in this paper.

For weak monochromatic freestream forcing waves, the generation of instability waves are expected to be linear with respect to the forcing amplitudes for the disturbances with the same fundamental frequency. Figure 21 shows the maximum temperature amplitudes of the first and second modes as functions of the freestream forcing disturbance amplitudes for the case of A.1. The dotted lines are the expected linear response to the freestream forcing amplitudes. The figure shows that when ϵ is very small, the receptivity of the wave mode of the fundamental frequency is linear. As ϵ increases, the receptivity results deviate from the linear curves due to the nonlinear effects of the nonlinear interaction between the wave harmonics.

Figure 22 shows the temperature disturbance amplitudes along the body surface for two cases of ϵ at $F = 2655$. Both the fundamental mode ($n = 1$), second harmonic ($n = 2$), and mean flow distortion ($n = 0$) for the two cases are plotted in the figure. The scaled results of the two cases should be the same for linear modes. The figure shows that receptivity of the fundamental modes are governed by linear mechanism, while the second harmonic and the mean flow distortion is nonlinear with respect to ϵ as shown by the figure.

For the leading edge receptivity problems of hypersonic flows over blunt bodies, the effects of nose bluntness can be characterized by the nondimensional Strouhal number defined in Eq. (7). Therefore, the increase of forcing frequency at a fixed nose radius is equivalent to the increase of nose bluntness. We investigate the effects of forcing frequencies and nose bluntness on the receptivity of a hypersonic leading edge by considering a number of test cases with a range of forcing frequencies F while holding all other flow parameters fixed. The specific nondimensional frequencies are in the range of $F = 531$ to 2655, which corresponds to the Strouhal number in the range of $S = 0.4$ to 2.

Figure 23 shows the distribution of the amplitudes of horizontal velocity and entropy perturbations along a grid line near the body surface for Cases A.1 to A.7 of different forcing frequencies. Each line in the figure represents a test case of different frequency. The results of different frequencies show similar receptivity pattern that first modes grow and decay, followed by the growth and decay of second and third modes respectively. As frequency decreases, the maximum first mode growth becomes larger, its location moves downstream, and the first mode instability region extends to a much longer range. The second mode instability region appears at further downstream to the first mode region with higher local Reynolds numbers. Similar to the first mode cases, the second mode increases in strength as frequency decreases, though they are weaker than the first mode region for these particular flow conditions.

The receptivity effects are often measured by a receptivity coefficient. For incompressible boundary layer receptivity studies, it is defined by the ratio of amplitudes at the Branch I neutral stability point to the freestream wave amplitudes. Such a definition is difficult to ap-

ply to current hypersonic boundary layer receptivity. Therefore, a different receptivity coefficient for hypersonic receptivity studies is defined as

$$A = \frac{|q'|_{max}}{M_\infty \epsilon} \tag{30}$$

where $|q'|_{max}$ is the Fourier amplitude for a flow variable q at a location of maximum first or second mode amplitudes in the boundary layer.

Figure 24 shows the variation of receptivity coefficient $|A|$ defined by entropy perturbations as a function of F. The results of A for both the first and the second modes are plotted in the same figure. As the frequency decreases, the receptivity coefficients for the first modes increase and approach peak values. The location of the maximum first and second mode wave amplitudes as a function of F is shown in Fig. 25 The frequency increase corresponds to the increase of the Strouhal number and the relative nose radius. Therefore, as the relative nose radius increases, the receptivity coefficients decrease.

6.2 Case B: Freestream Entropy Waves

In addition to freestream acoustic waves, other forms of disturbances in the freestream can also affect the instability in hypersonic boundary layers. In this section, the results of receptivity of hypersonic boundary layers to single-frequency planar entropy waves in the freestream are considered. Freestream entropy waves represent non-acoustic temperature or density perturbations in the freestream of the flow field.

For hypersonic flow over a blunt leading edge, the bow shocks play an important role in the leading edge receptivity process. Before entering a hypersonic boundary layer, a freestream disturbance wave will interact with the bow shock first. The interaction of any kind of disturbances with a shock wave will produce all three kinds of waves: acoustic, entropy and vorticity waves. It is these generated disturbances which propagate or convect downstream to enter the boundary layers. The strengths of the generated waves behind the shock depend on the specific incident wave from the freestream.

The linear interaction of freestream disturbance wave with a planar shock can be predicted by linear theory such as that derived by Mckenzie and Westphal [25]. For the case of the transmission of freestream acoustic waves through a normal shock, the ratio of pressure amplitudes before and after the shock is:

$$\frac{p'_s}{p'_\infty} = \frac{2M_\infty^4 + 2(\gamma+1)M_\infty^3 + 2(3\gamma-1)M_\infty^2 + 1 - \gamma}{(\gamma+1)(1+M_\infty^2+2M_\infty^2 M_s)} \tag{31}$$

where subscript s represents variable immediately behind the shock. The corresponding generation formula for the case of freestream entropy wave is

$$\frac{p'_s}{s'_\infty} = -\frac{2\gamma M_\infty^2 (M_\infty^2 - 1)}{(\gamma+1)[1+M_\infty^2(1+M_\infty^2(1+2M_s))]} \tag{32}$$

The strength of freestream acoustic and entropy waves are measured by $p'_\infty = \epsilon M_\infty$ and $s'_\infty = \epsilon M_\infty$ respectively. Table 1 shows a comparison of pressure and entropy amplitudes behind a shock generated by incident acoustic waves with those generated by incident entropy waves for the same freestream wave amplitudes for the current case of Mach 15 flow with $\gamma = 1.4$. For the same wave strength in the freestream, freestream acoustic waves generate stronger acoustic wave components behind the bow shock while generating weaker entropy wave components. Therefore, freestream acoustic and entropy receptivity cases represents the effects of receptivity by an acoustic wave dominated perturbations behind the shock as compared to the entropy wave dominated ones. Therefore, a comparison of the results of acoustic and entropy wave receptivity will help to understand the relative importance of the two kinds of perturbations in the freestream on generating instability waves in the boundary layers.

Table 1. Linear Generation Coefficients by Freestream Waves ($M_\infty = 15, \gamma = 1.4$)

Incident Waves	$\frac{p_2}{\epsilon M_\infty \gamma p_2}$	$\frac{s'_2}{\epsilon M_\infty c_p}$	$\frac{\rho'_2}{\epsilon M_\infty \rho_2}$
Acoustic	0.4715614	-0.5123659	0.9839273
Entropy	-0.4022472	0.6099873	-1.012235

The flow conditions for the entropy receptivity Case B are listed in Section 4. All cases in group B have the same base steady solution as that of Case A except that the freestream is planar entropy waves.

Figure 26 shows the contours of instantaneous perturbations of horizontal velocity components for Case B.1 of freestream entropy wave of $F = 2655$. The u' contours of the entropy Case B.1 show wave patterns in the boundary layer very similar to those of Case A.1 for freestream acoustic waves (Fig. 11). Specifically, it shows a first mode growth and decay in the region of $x < 0.2$, followed by a second mode structure in the region of $x > 0.2$. The contours of Fourier amplitudes and phase angles of horizontal velocity components for the same case are shown in Fig. 27. The wave patterns inside the boundary layer near the wall are identical to those of freestream acoustic waves at the same frequency (Fig. 14), though the wave patterns generated by the two kinds of freestream waves are different in the region I outside of the boundary layer. The results indicate that freestream perturbations of the same frequency but different kinds generate identical boundary layer wave modes, which is independent of the forcing disturbances.

Figure 28 compares the pressure and temperature amplitudes of two case of freestream waves along a wall-normal grid line. Since the amplitudes of the two cases are different, the wave amplitudes in the figure are normalized by their own first peak values near the

wall so that we can compare the eigenfunctions. The numbers marked on the figures are those for the case of freestream acoustic waves of Case A.1. The figure shows that while the wave strengths are very much different outside the boundary layers, the induced instability wave modes in the wall are identical.

Figure 29 shows the distribution of the Fourier amplitudes of $|u'|$ along a grid line near the parabola surface for the acoustic and entropy cases. The figure shows that the freestream acoustic wave generates stronger first and second wave modes in the boundary layer than the freestream entropy wave does. Meanwhile, the location of the peak in the first mode and the second mode are the same for two cases. Figure 30 shows the corresponding distribution immediately behind the bow shock. The freestream entropy waves generate stronger entropy perturbations behind the shock but weaker pressure perturbations near the leading edge. These results show that acoustic waves play a more important role in the receptivity process of exciting the instability waves in the boundary layer.

Figures 31 shows the variation of local pressure and entropy perturbation amplitudes along the stagnation line for Cases A.1 and B.1. Again, freestream acoustic waves generate stronger perturbations in the boundary layer though it induces weaker entropy perturbation immediately behind the shock. Both pressure and entropy perturbations are stronger for the acoustic case A.1.

Figure 32 shows the distribution of the amplitudes of horizontal velocity and entropy perturbations along a grid line near the body surface for Case B of different forcing frequencies. Each line in the figure represents a test case of different frequency. The results of different frequencies show similar receptivity patterns as those for the freestream acoustic wave cases (Fig. 23), except that the entropy waves induce weaker perturbations in the boundary layer. Figure 33 compares the variation of receptivity coefficient $|A|$ induced by freestream acoustic and entropy waves. The corresponding comparison of location of maximum entropy amplitude between the cases of freestream acoustic and entropy waves are shown in Fig. 34. Again the receptivity coefficients for freestream entropy waves are weaker than those for acoustic waves, but the location of maximum wave amplitudes are the same for both cases. Figure 33 also shows that as the frequency decreases, the receptivity coefficients for the first modes increase, approach a peak value, and decrease as F is further reduced. Therefore, as the relative nose radius decreases, the receptivity coefficients will first increase, but decrease if the nose radius is further decreased.

6.3 Case C: Effects of Wall Temperatures

It has been shown by LST [26] that wall cooling stabilizes the first mode in a flat plate boundary layer while destabilizing the second mode. The wall-cooling effects on the leading edge receptivity are studied by DNS of acoustic receptivity for two cases of wall temperatures in Case A ($T_w = 1000K$) and Case C ($T_w = 2000K$). The flows conditions for the higher wall temperature Case C are listed in Section 4.

Figure 35 shows the contours of instantaneous perturbations and Fourier amplitudes of horizontal velocity components for the case of freestream acoustic waves with $T_w = 2000K$ and $\epsilon = 5 \times 10^{-4}$. The u' contours of the current case show a very similar wave pattern in the boundary layer as to those of Case A.1 for lower wall temperature (Figs. 11 and 14).

Figure 36 compares the distributions of the Fourier amplitudes of $|s'|$, $|u'|$ and $|v'|$ along a grid line near the parabola surface for Case A.1 and C.1 of higher wall temperature. The figure shows that the wall cooling results in a stronger receptivity in wave perturbations in the boundary layer. Meanwhile, the location of the peak in the first mode and the second mode are not very sensitive to the changes in wall temperatures.

Figure 37 shows the distribution of the amplitudes of horizontal velocity and entropy perturbations along a grid line near the body surface for Case C of different forcing frequencies. Each line in the figure represents a test case of different frequency. The results of different frequencies show similar receptivity patterns as those for the freestream acoustic wave cases (Fig. 23), except that the case of high wall temperature induce weaker perturbations in the boundary layer.

Figures 38 and 39 compare the variation of receptivity coefficient $|A|$ induced by freestream acoustic waves for two cases of different wall temperatures. The corresponding comparisons of location of maximum entropy amplitude are shown in Fig. 40. Again the receptivity coefficients for the case of higher wall temperature are weaker but the location of maximum wave amplitudes are the very close for both cases.

6.4 Case D: Effects of Reynolds Numbers

The Reynolds number effects on receptivity are studied by DNS of two cases of acoustic receptivity of the same flow conditions except that the sizes of the parabola are different. The flow conditions for the higher Reynolds number Case D are listed in Section 4.

Figure 41 shows the contours of instantaneous perturbations of horizontal velocity components for the case of higher Reynolds numbers at $\epsilon = 5 \times 10^{-4}$. The u' contours of the current case show a generation of first mode instability waves in the boundary layer. Since the frequency for the current case is very low, only the first mode region is shown in the figure.

Figure 42 shows the distribution of the amplitudes of horizontal velocity and entropy perturbations along a grid line near the body surface for Case D of different forcing frequencies. Each line in the figure represents a

test case of different frequency. The results show that the case of high Reynolds numbers induce stronger perturbations in the boundary layer. In addition, the second mode also becomes stronger than the first for Case D.3. Figure 43 compares the variation of receptivity coefficient $|A|$ induced by freestream acoustic waves for two cases of different Reynolds numbers. Again, the receptivity coefficients for the case of higher Reynolds numbers are stronger but the location of maximum wave amplitudes are very close for both cases.

7 CONCLUSIONS

A parametric study of the leading-edge receptivity of a hypersonic boundary layer to freestream monochromatic planar acoustic and entropy disturbances has been carried out by direct numerical simulations (DNS) for a two-dimensional Mach 15 flow over a parabola. The steady flow solutions are studied with the focus on the vorticity interaction between inviscid vorticity field generated by the bow shock and viscous viscosity generation by the boundary layer. In the parametric studies, the effects of different freestream waves, wall temperatures, nose bluntness, and Reynolds number are investigated. The main conclusions are:

1. The freestream disturbances generated both boundary-layer first and second modes. The first mode is always generated near the leading edge and is amplified before decaying rapidly. The second mode is the dominant mode after the first mode decay. The eigenfunctions of the first and second modes obtained by LST agree well with the DNS results inside the boundary layers. The agreement becomes better as the waves propagate downstream.

2. The results show that the receptivity coefficients and the region of the first mode instability increases substantially when the forcing frequencies decrease. As the forcing frequencies decrease further, the receptivity coefficients reach a peak and becomes smaller afterward. These results indicate that the receptivity coefficients increase as the relative nose radius decreases but there is a critical nose bluntness (or frequency) which corresponds to maximum receptivity coefficients.

3. The DNS shows the generation of instability modes of the fundamental forcing frequency is linear. The receptivity also generates nonlinear superharmonics.

4. The results show that wall cooling increases the receptivity coefficients or wave perturbations generated in the boundary layers.

5. The increase in freestream Reynolds numbers shows an increase in receptivity coefficients.

ACKNOWLEDGMENTS

This research was supported by the Air Force Office of Scientific Research under grant numbers F49620-97-1-0030 and F49620-00-1-0101 monitored by Dr. Len Sakell.

References

[1] National Research Council (U.S.). Committee on Hypersonic Technology for Military Application, "Hypersonic Technology for Military Application," *Technical Report*, Vol. National Academy Press, Washington, DC., 1989.

[2] Defense Science Board, "Final Report of the Second Defense Science Board Task Force on the National Aero-Space Plane (NASP)," *AD-A274530, 94-00052, November*, 1992.

[3] Herbert, T. and Morkovin, M. V., "Dialogue on Bridging Some Gaps in Stability and Transition Research," *Laminar-Turbulent Transition, IUTAM Symposium, Stuttgart, Germany, Springer-Verlag Berlin*, edited by R. Eppler and H. Fasel, 1980, pp. 47–72.

[4] Morkovin, M. V. and Reshotko, E., "Dialogue on Progress and Issues in Stability and Transition Research," *Laminar-Turbulent Transition, IUTAM Symp., Toulouse, Springer-Verlag*, edited by D. Arnal and R. Michel, 1990, pp. 3–30.

[5] Reshotko, E., "Boundary Layer Instability, Transition and Control," *AIAA paper 94-0001*, 1996.

[6] Herbert, T., "Progress in Applied Transition Analysis," *AIAA paper 96-1993*, Vol. 27th AIAA Fluid Dynamics Conference, New Orleans, LA, June, 1996.

[7] Bushnell, D., "Notes on Initial Disturbance Field for the Transition Problem," *Instability and Transition, Vol. I*, Vol. M. Y. Hussaini and R. G. Viogt, editors, pp. 217-232, Springer-Verlag, 1990.

[8] Nishioka, M. and Morkovin, M. V., "Boundary-Layer Receptivity to Unsteady Pressure Gradients: Experiments and Overview," *Journal of Fluid Mechanics*, Vol. 171, pp. 219-261 1986.

[9] Goldstein, M. E. and Hultgren, L. S., "Boundary-Layer Receptivity to Long-Wave Free-Stream Disturbances," *Annual Review of Fluid Mechanics*, Vol. 21, pp. 137-166 1989.

[10] Saric, W. S., Reed, H. L., and Kerschen, E. J., "Leading Edge Receptivity to Sound: Experiments, DNS, and Theory," *AIAA Paper 94-2222*, 1994.

[11] Reshotko, E., "Hypersonic Stability and Transition," *in Hypersonic Flows for Reentry Problems, Eds. J.-A. Desideri, R. Glowinski, and J. Periaux, Springer-Verlag*, Vol. 1, 1991, pp. 18–34.

[12] Morkovin, M. V., "Transition at Hypersonic Speeds," *ICASE Interim Report 1*, Vol. NASA CR 178315, May, 1987.

[13] Zhong, X., "Direct Numerical Simulation of Hypersonic Boundary-Layer Transition Over Blunt Leading Edges, Part I: New Numerical Methods and Validation (Invited)," *AIAA paper 97-0755, 35th AIAA Aerospace Sciences Meeting and Exhibit, January 6-9, Reno, Nevada*, 1997.

[14] Zhong, X., "Direct Numerical Simulation of Hypersonic Boundary-Layer Transition Over Blunt Leading Edges, Part II: Receptivity to Sound (Invited)," *AIAA paper 97-0756*, January 1997.

[15] Zhong, X., "High-Order Finite-Difference Schemes for Numerical Simulation of Hypersonic Boundary-Layer Transition," *Journal of Computational Physics*, Vol. 144, August 1998, pp. 662–709.

[16] Zhong, X. and Joubert, X., "Bow-Shock/Disturbance Interaction for Hypersonic Flow over a Cylinder," *Shock Waves*, edited by B. Sturtevant, J. E. Shepherd, and H. G. Hornung, World Scientific, Singapore, 1996.

[17] Truesdell, C., "On the curved shocks in steady plane flow of an ideal fluid," *Journal of Aero. Sciences*, Vol. 19, 1952, pp. 826–828.

[18] Lighthill, M. J., "Dynamics of a Dissociating Gas. Part I. Equilibrium Flow," *Journal of Fluid Mechanics*, Vol. 2, No. 1, 1957, pp. 1.

[19] Hayes, W. D., "The vorticity jump across a gasdynamic discontinuity," *Journal of Fluid Mechanics*, Vol. 26, 1957, pp. 433–436.

[20] Hornung, H. G., "Gradients at a curved shock in reacting flow," *Shock Waves*, June 1997.

[21] Serrin, J., "Mathematical Principles of Classical Fluid Mechanics," *Handbuch Der Physik, edited by S. Flygge and C. Truedell*, Vol. VIII/1, 1959, pp. 125–350.

[22] Lees, L., "Laminar Heat Transfer Over Blunt-Nosed Bodies at Hypersonic Flight Speeds," *Journal of American Rocket Society*, April 1956, pp. 259–269.

[23] Fay, J. A. and Riddell, F. R., "Theory of Stagnation Point Heat Transfer in Dissociated Air," *Journal of the Aeronautical Sciences*, Vol. 25, 1958, pp. 73–85.

[24] Hu, S. H. and Zhong, X., "Linear Stability of Compressible Couette Flow," *AIAA paper 97-0432*, January 1997.

[25] Mckenzie, J. F. and Westphal, K. O., "Interaction of Linear Waves with Oblique Shock Waves," *The Physics of Fluids*, Vol. 11, No. 11, November 1968, pp. 2350–2362.

[26] Mack, L. M., "Boundary Layer Linear Stability Theory," *AGARD report, No. 709*, 1984, pp. 3–1 to 3–81.

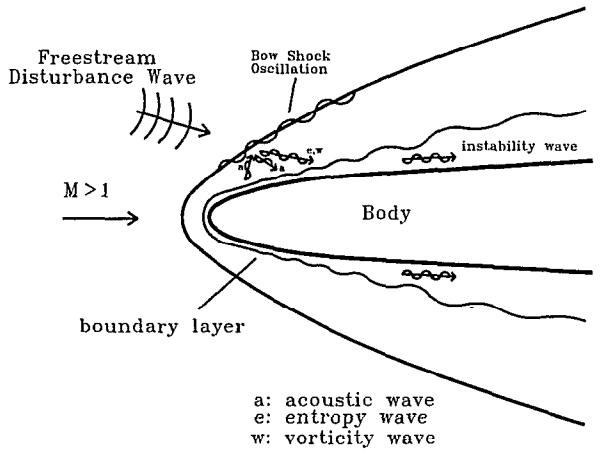

Figure 1: A schematic of the wave field of the interaction between the bow shock and free-stream disturbances. The disturbances can originate either from the freestream, surface roughness, or surface vibrations.

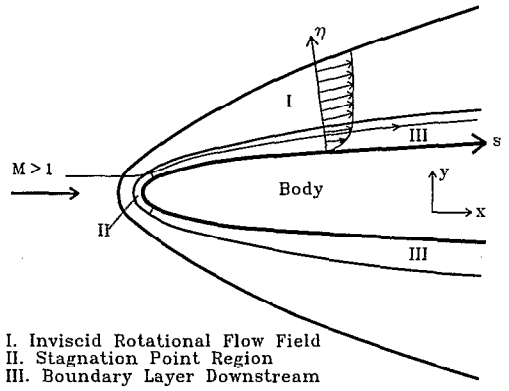

Figure 2: Flow field of viscous hypersonic flow over a blunt leading edge.

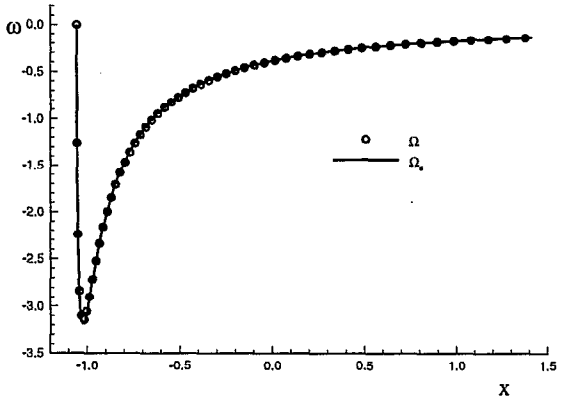

Figure 3: Distribution of local vorticity immediately behind the bow shock as a function of x for Case A (Ω: solutions of the full Navier-Stokes equations; Ω_s: theoretical prediction).

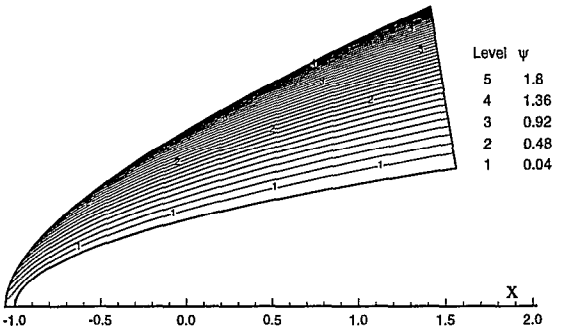

Figure 4: Steady flow streamlines for Case A.

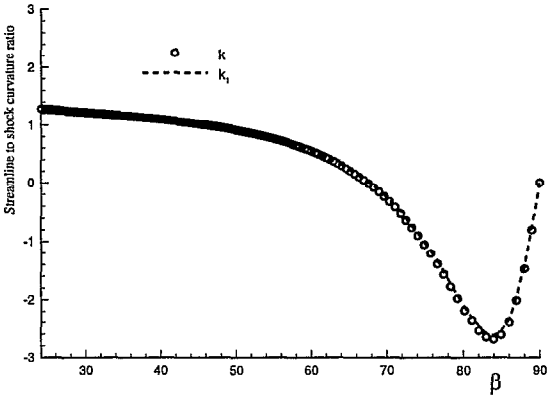

Figure 5: Streamline to shock curvature ratios as a function of local shock angle for Case A (k: Navier-Stokes solutions, k_1: theoretical results by Hornung 1997).

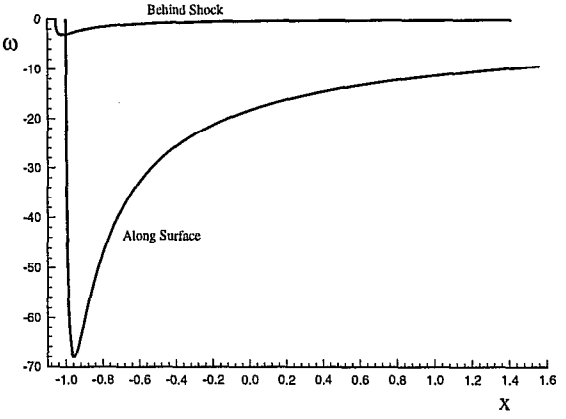

Figure 6: Steady vorticity distribution along the body surface and behind the bow shock vs. x for Case A.

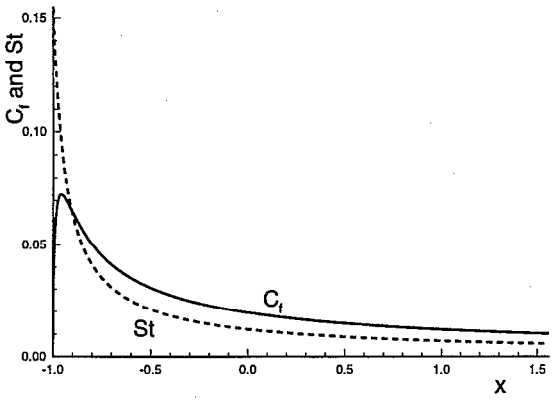

Figure 7: Distribution of Navier-Stokes solutions of skin friction coefficient ($C_f = \frac{\tau^*}{\rho^*_\infty u^{*2}_\infty/2}$) and heat transfer coefficient ($St = \frac{q^*}{\rho^*_\infty u^*_\infty (h^*_0 - h^*_w)}$) along the body surface for Case A.

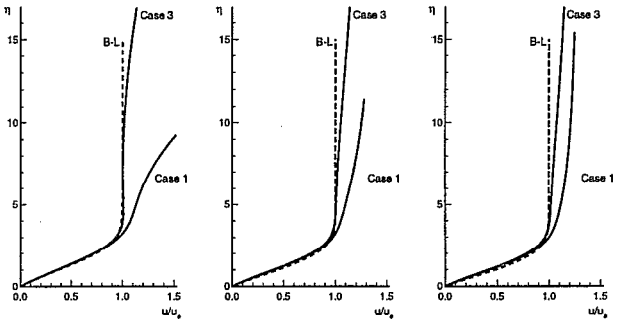

Figure 9: Distribution of streamwise velocity components in the wall normal direction in local boundary layer similarity coordinates η (Case 1: Case A, Re_∞ = 6026.6; Case 3: Case D, Re_∞ = 60266; B-L: boundary layer solutions).

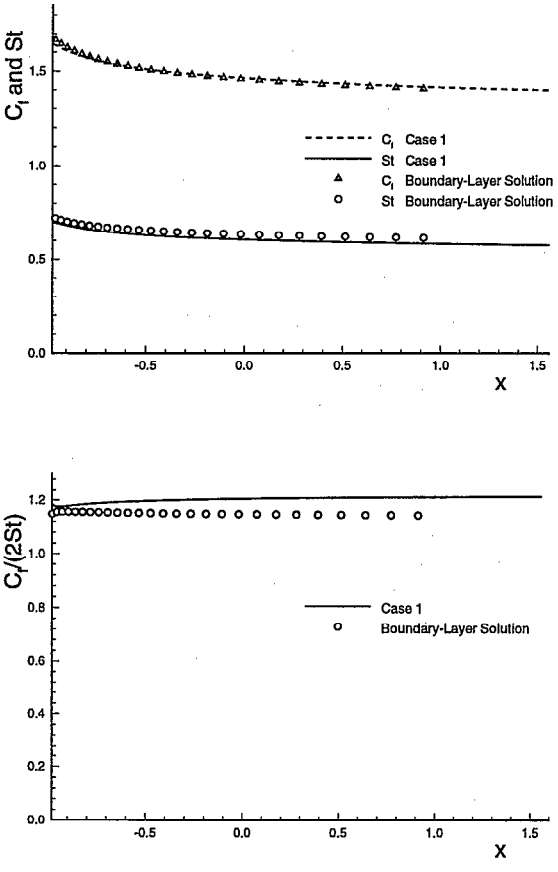

Figure 8: Distribution of locally defined skin friction coefficient c_f and heat transfer coefficient st along the body surface for Case A (Case 1).

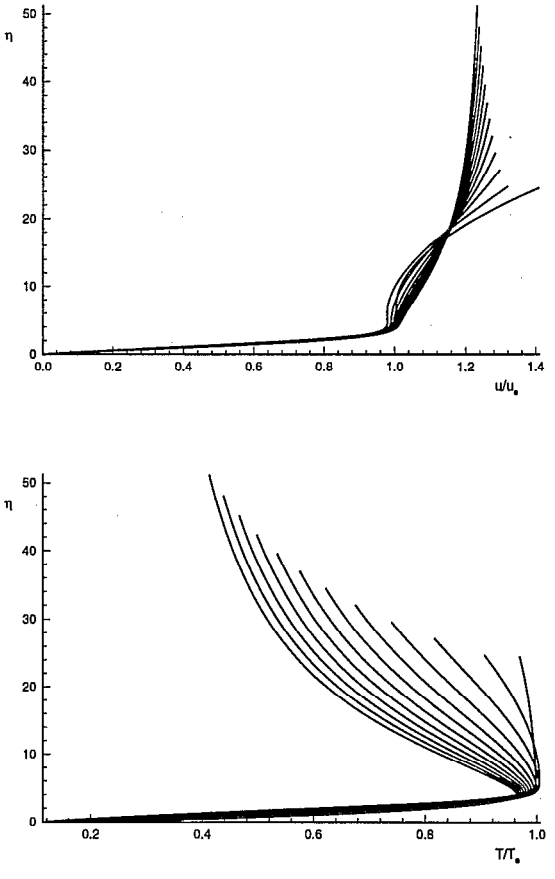

Figure 10: Distribution of streamwise velocity and temperature components in the wall normal direction in local boundary layer similarity coordinates η at several i grid stations for Case D.

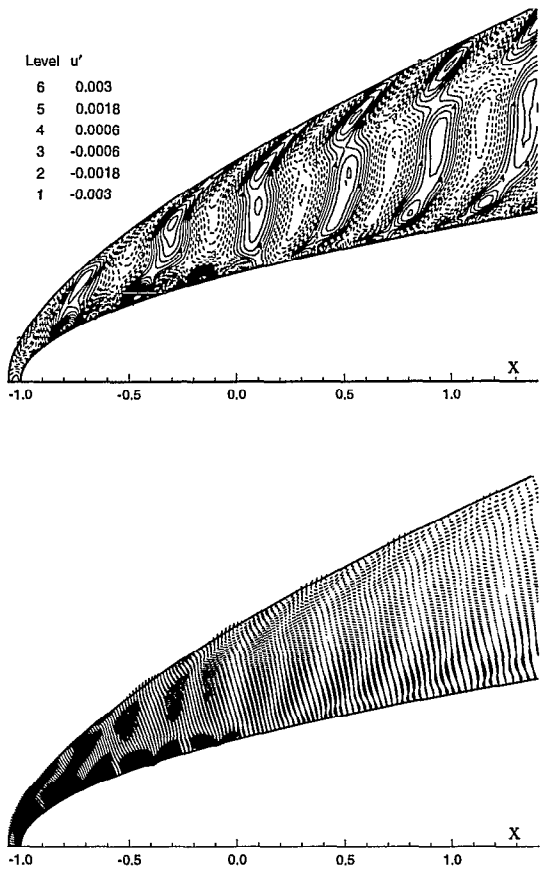

Figure 11: Contours of instantaneous perturbation of velocity components u' and velocity vectors after the solutions reach a time periodic state for Case A.1 at $\epsilon = 5 \times 10^{-4}$.

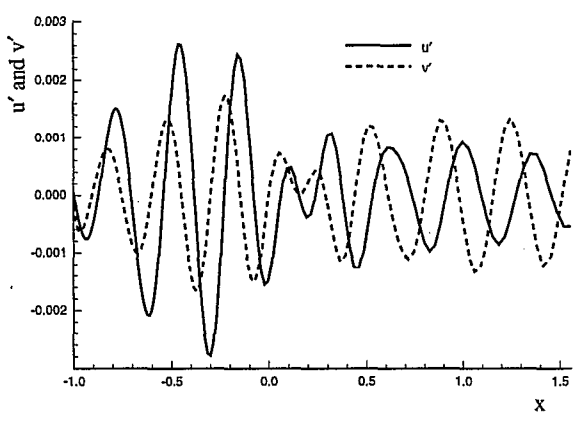

Figure 12: Distribution of instantaneous perturbation of horizontal velocity components in the boundary layer along the $j = 30$ grid lines near the body surface for Case A.1 at $\epsilon = 5 \times 10^{-4}$.

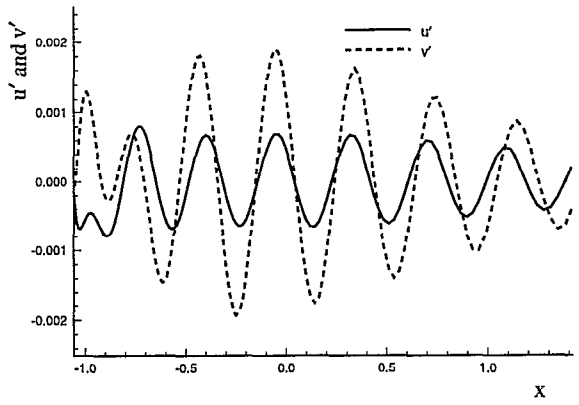

Figure 13: Distribution of instantaneous perturbation of horizontal velocity components immediately behind the shock for Case A.1 at $\epsilon = 5 \times 10^{-4}$.

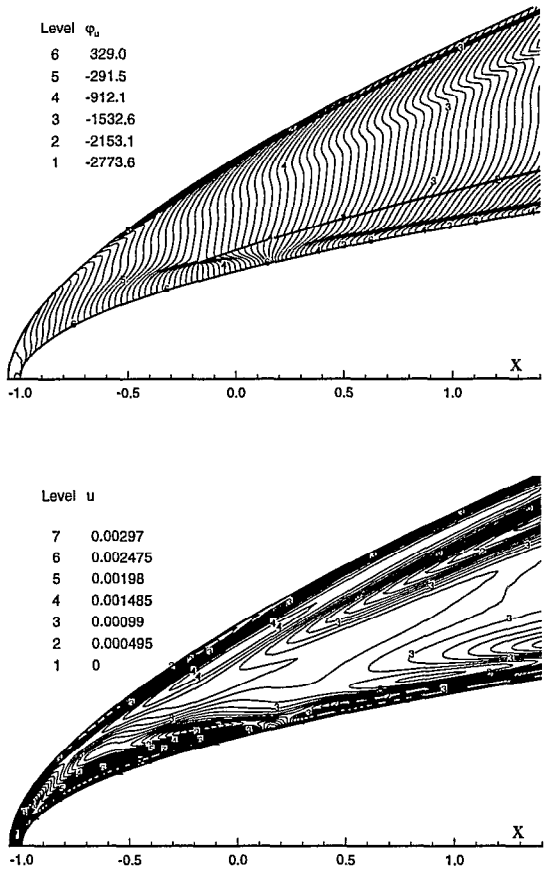

Figure 14: Contours of Fourier amplitudes and Fourier phase angles (in degrees) of horizontal velocity components $|u'|$ for Case A.1 at $\epsilon = 5 \times 10^{-4}$.

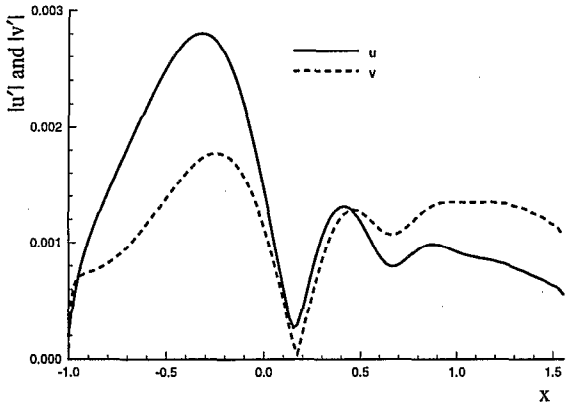

Figure 15: Distribution of the Fourier amplitudes of the velocity perturbations in the boundary layer along the $j = 30$ grid line near the parabola surface for Case A.1 at $\epsilon = 5 \times 10^{-4}$.

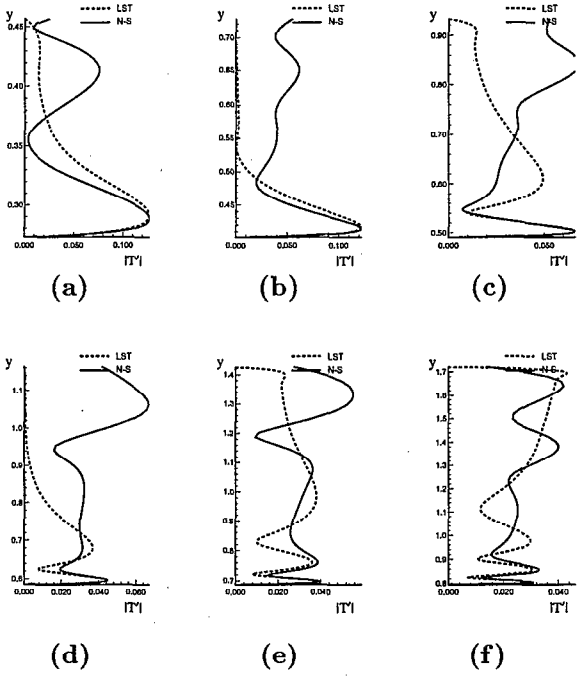

Figure 17: Variation of the temperature amplitude along grid lines normal to parabola surface at six i grid stations for Case A.1 at $\epsilon = 5 \times 10^{-4}$. (a) $i = 50$ LST: 1st mode, (b) $i = 80$ LST: 1st mode, (c) $i = 100$ LST: 2nd mode, (d) $i = 120$ LST: 2nd mode, (e) $i = 140$ LST: 3rd mode, (f) $i = 160$ LST: 3rd mode.

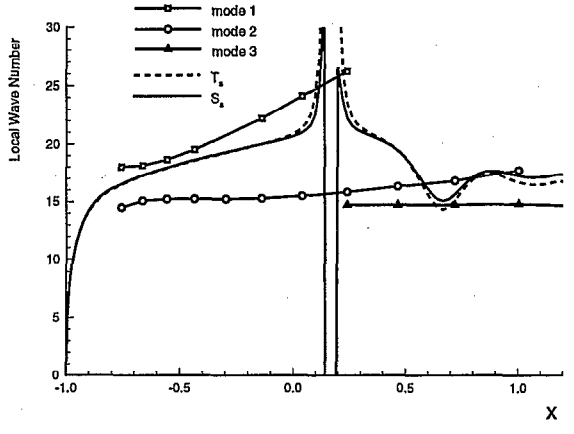

Figure 16: Distribution of the local wave numbers in the boundary layer along the $j = 30$ grid line near the parabola surface for Case A.1 at $\epsilon = 5 \times 10^{-4}$.

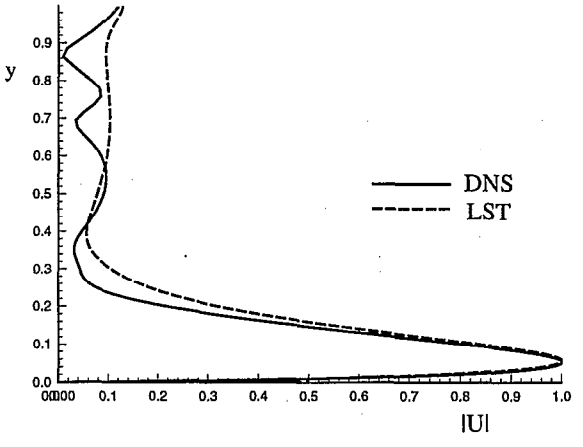

Figure 18: First-mode eigenfunction amplitudes along the wall-normal direction at $x = 0.5521$ for Case A.3 at $\epsilon = 5 \times 10^{-4}$.

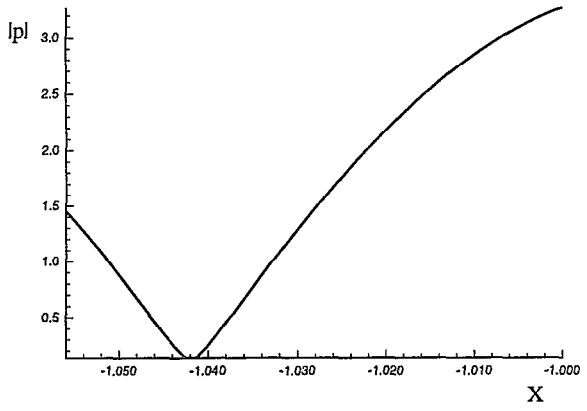

Figure 19: Variation of local pressure perturbation amplitudes along the stagnation line for Case A.1 at $\epsilon = 5 \times 10^{-4}$.

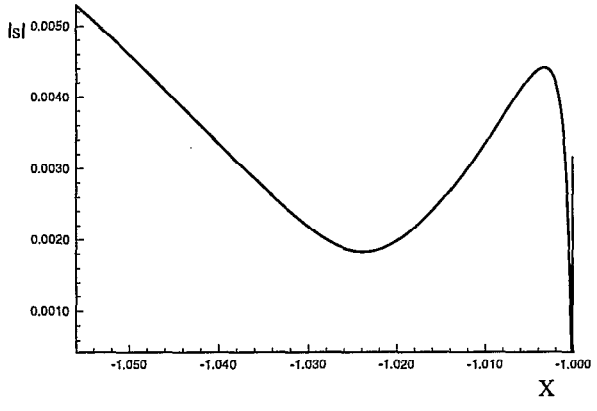

Figure 20: Variation of local entropy perturbation amplitudes along the stagnation line for Case A.1 at $\epsilon = 5 \times 10^{-4}$.

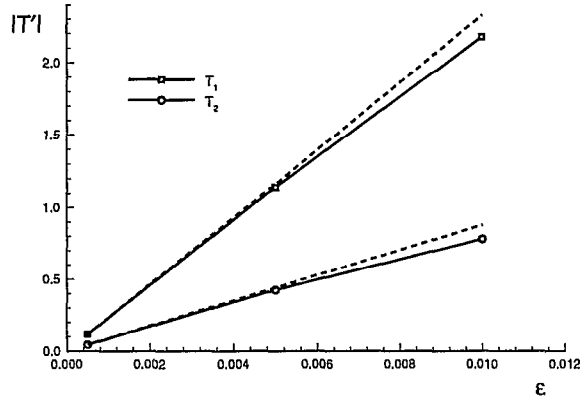

Figure 21: Maximum temperature amplitudes of the first mode (T_1) and second mode (T_2) vs. freestream forcing disturbances amplitudes ϵ for Case A.1.

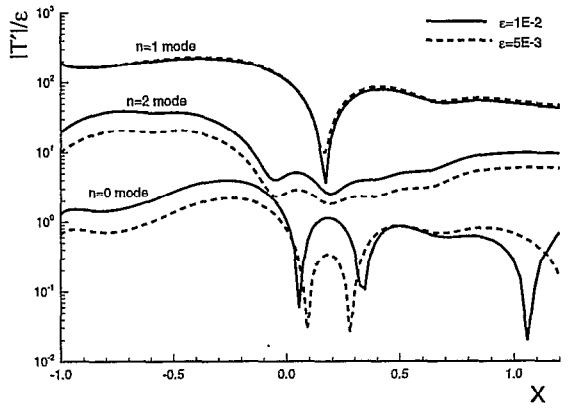

Figure 22: Distribution of amplitudes of temperature perturbations in the boundary layer along the $i = 30$ grid line near the body surface for Case A.1 at two sets of ϵ.

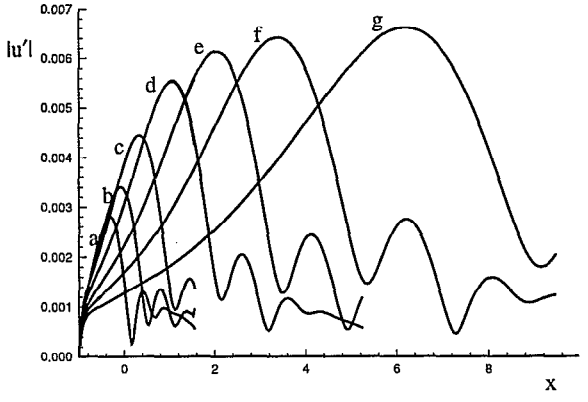

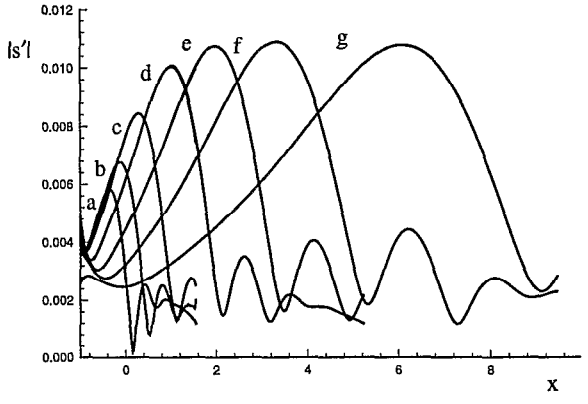

Figure 23: Variation of horizontal velocity and entropy perturbation amplitudes along the $i = 30$ grid line near the body surface with several forcing frequencies with $\epsilon = 5 \times 10^{-4}$ (Cases a to g in the figure correspond to Case A.1 to A.7 respectively)

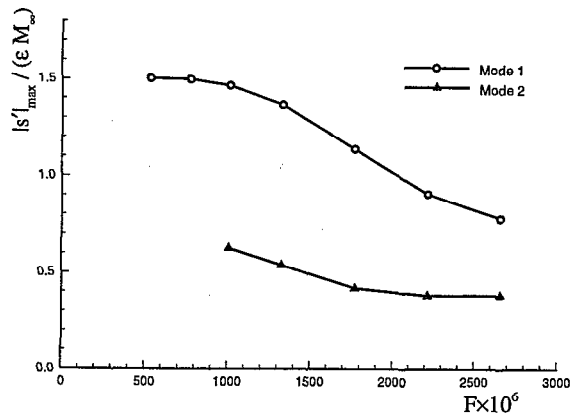

Figure 24: Variation of the amplitude of receptivity coefficient $|A|$ vs. forcing disturbance frequency for Case A of freestream acoustic waves with $\epsilon = 5 \times 10^{-4}$.

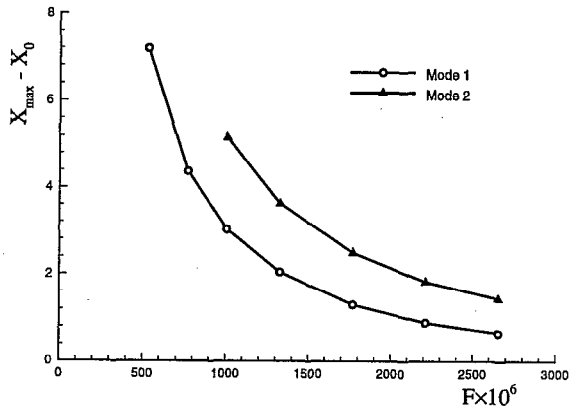

Figure 25: Location of maximum entropy amplitude vs. disturbance frequency for Case A of freestream acoustic waves with $\epsilon = 5 \times 10^{-4}$.

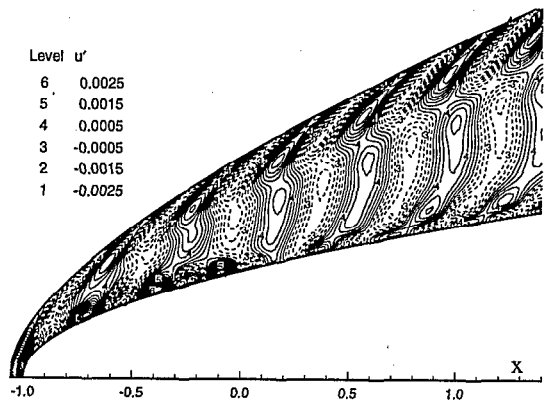

Figure 26: Contours of instantaneous perturbations of horizontal velocity components for Case B.1 of freestream entropy waves with $\epsilon = 5 \times 10^{-4}$.

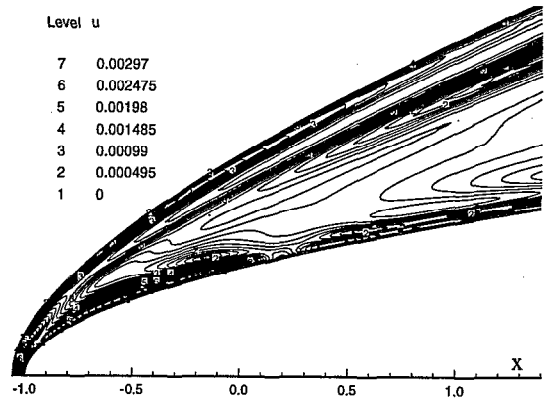

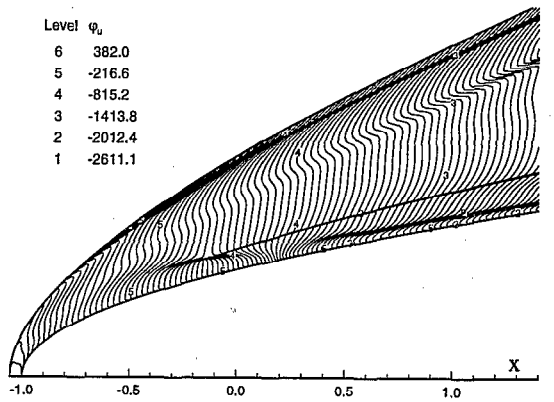

Figure 27: Contours of Fourier amplitudes and phase angles of horizontal velocity components for Case B.1 with $\epsilon = 5 \times 10^{-4}$.

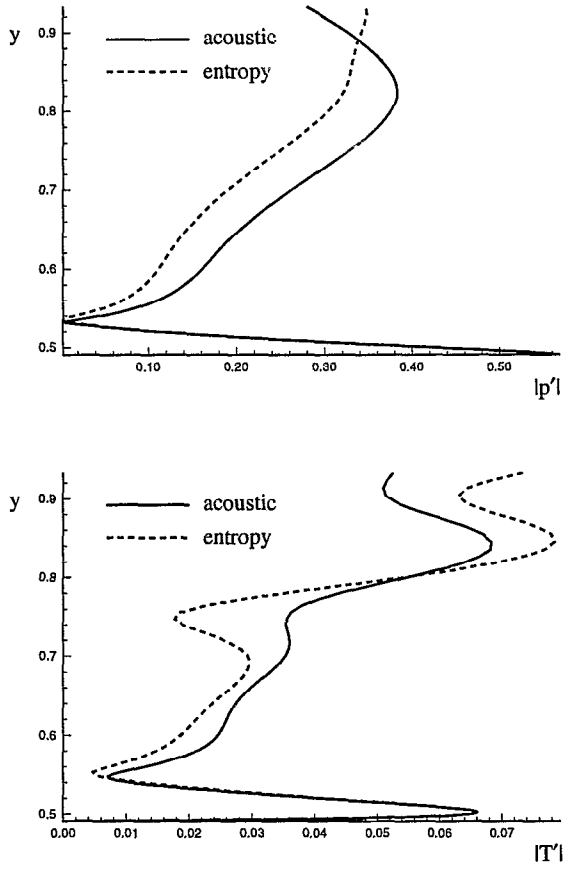

Figure 28: Variation of pressure and temperature amplitudes along the $i = 100$ grid line normal to the parabola surface for two cases of freestream waves at $F = 2655$ and $\epsilon = 5 \times 10^{-4}$ (acoustic: Case A.1, entropy: Case B.1).

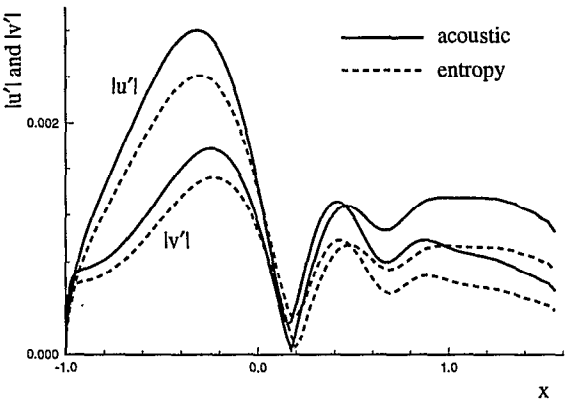

Figure 29: Distribution of the Fourier amplitudes of the horizontal velocity perturbations along the $j = 30$ grid line near the parabola surface for two cases of freestream waves at $F = 2655$ and $\epsilon = 5 \times 10^{-4}$ (acoustic: Case A.1, entropy: Case B.1).

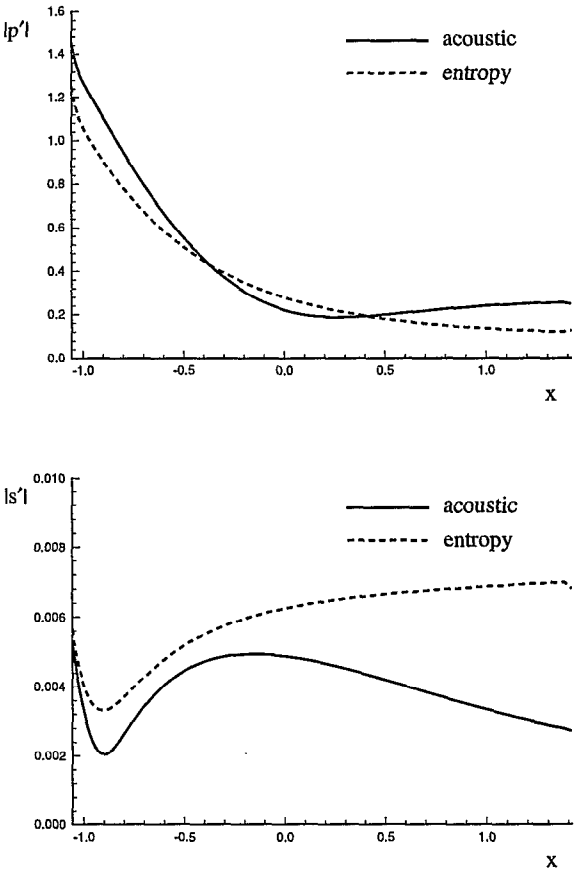

Figure 30: Distribution of the Fourier amplitudes of the pressure and entropy perturbations immediately behind the bow shock for two cases of freestream waves at $F = 2655$ and $\epsilon = 5 \times 10^{-4}$ (acoustic: Case A.1, entropy: Case B.1).

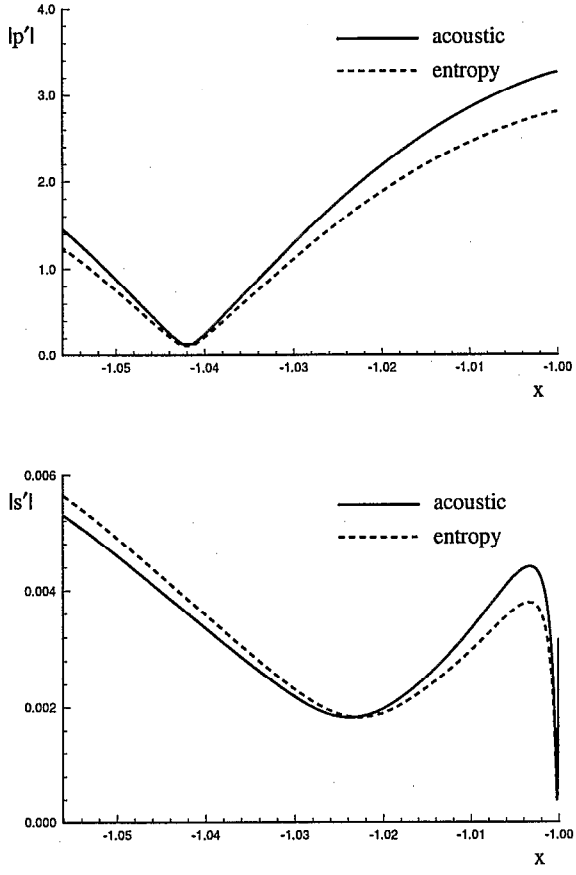

Figure 31: Distribution of the Fourier amplitudes of the pressure and entropy perturbations along the stagnation line of the flow field for two cases of freestream waves at $F = 2655$ and $\epsilon = 5 \times 10^{-4}$ (acoustic: Case A.1, entropy: Case B.1).

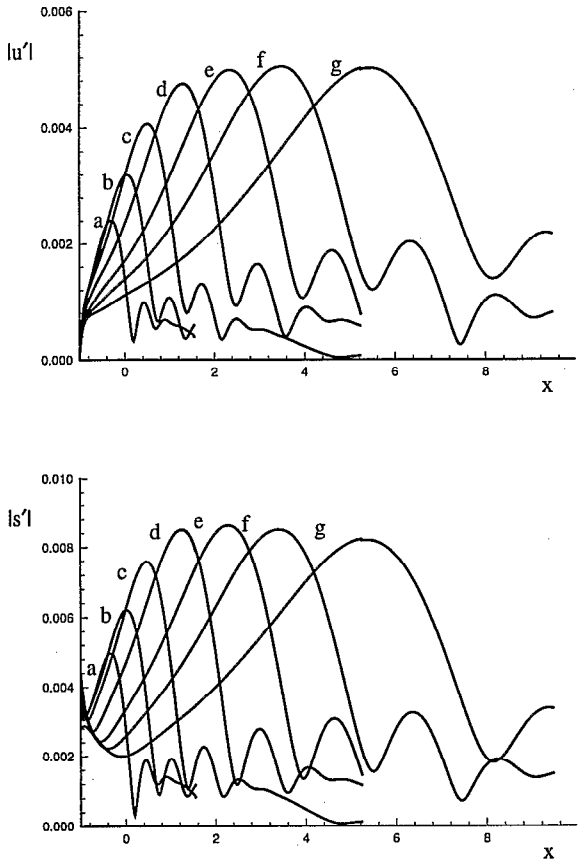

Figure 32: Variation of horizontal velocity and entropy perturbation amplitudes along the $i = 30$ grid line near the body surface with several forcing frequencies with $\epsilon = 5 \times 10^{-4}$ (Cases a to g in the figure correspond to Case B.1, B.3, ..., B.8 respectively).

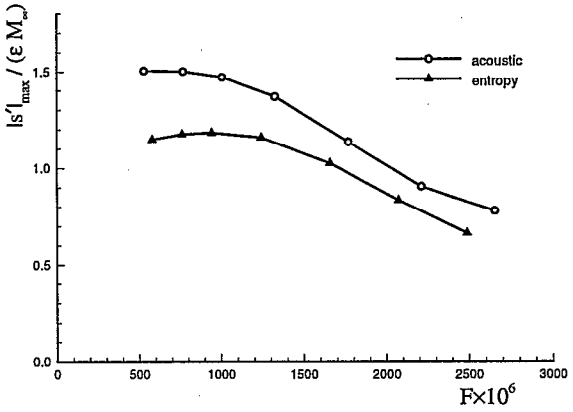

Figure 33: Comparison of variation of amplitude of receptivity coefficient $|A|$ vs. forcing disturbance frequency between the cases of freestream acoustic and entropy waves with $\epsilon = 5 \times 10^{-4}$ (acoustic: Case A; entropy: Case B).

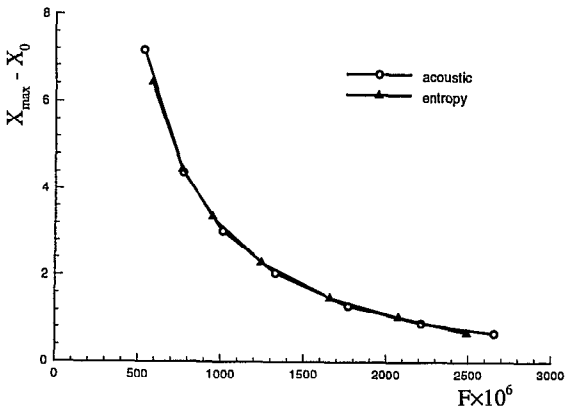

Figure 34: Comparison of location of maximum entropy amplitude vs. disturbance frequency between the cases of freestream acoustic and entropy waves with $\epsilon = 5 \times 10^{-4}$ (acoustic: Case A; entropy: Case B).

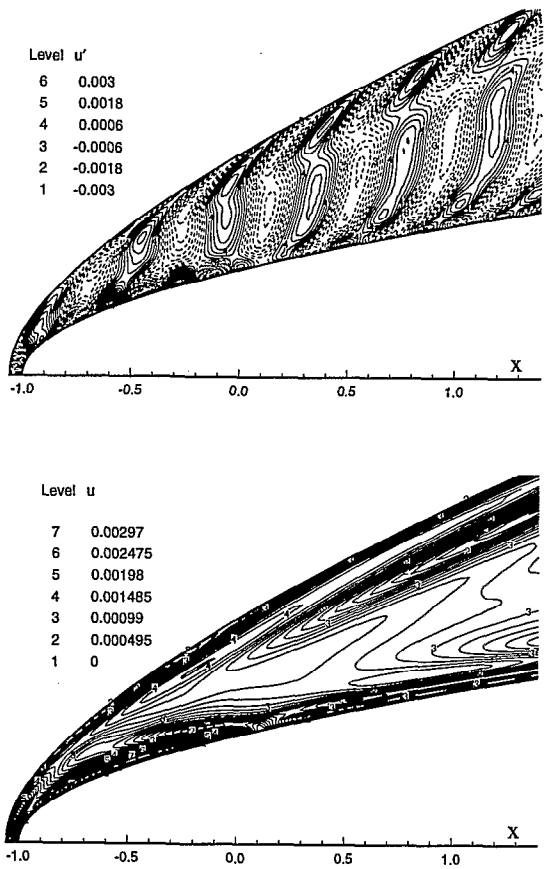

Figure 35: Contours of instantaneous perturbations and Fourier amplitudes of horizontal velocity components for Case C.1 with wall temperature $T_w = 2000K$ and $\epsilon = 5 \times 10^{-4}$.

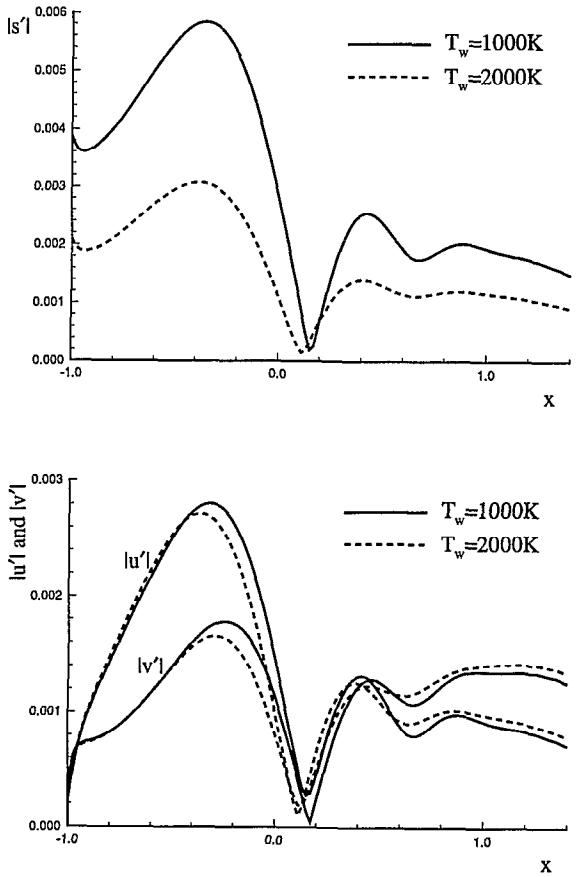

Figure 36: Distribution of the Fourier amplitudes $|s'|$, $|u'|$ and $|v'|$ along the $j = 30$ grid line near the parabola surface for two cases of different wall temperatures at $\epsilon = 5 \times 10^{-4}$ ($T_w = 1000K$: Case A.1; $T_w = 2000K$: Case C.1).

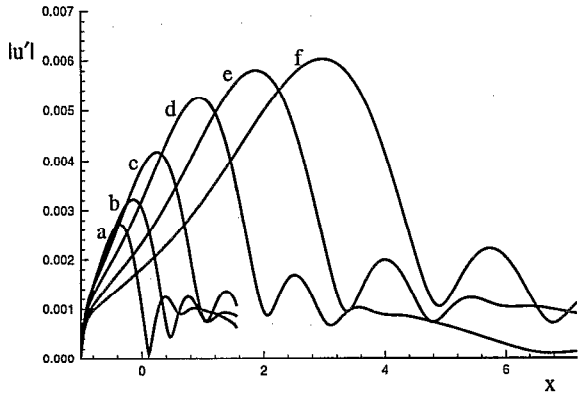

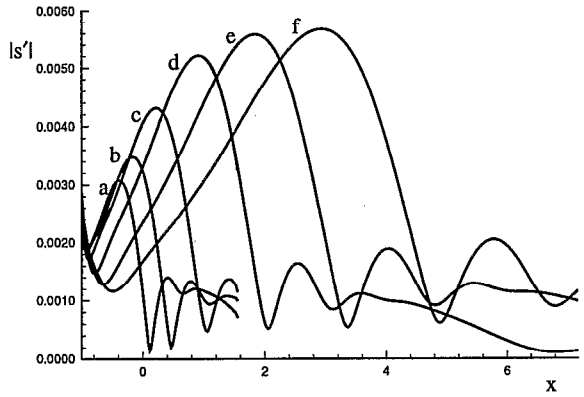

Figure 37: Variation of horizontal velocity and entropy perturbation amplitudes along the $i = 30$ grid line near the body surface with several forcing frequencies with $\epsilon = 5 \times 10^{-4}$ and $T_w = 2000K$ (Cases a to f in the figure correspond to Case C.1 to C.6 respectively).

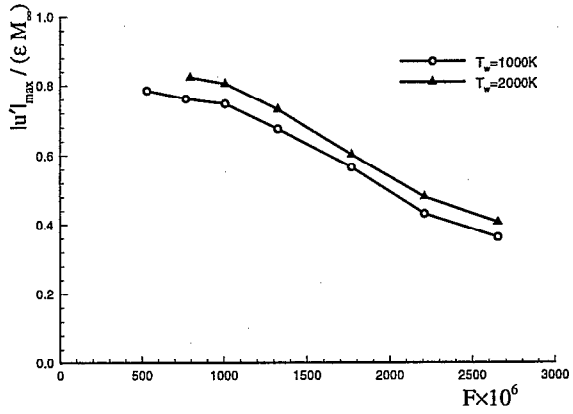

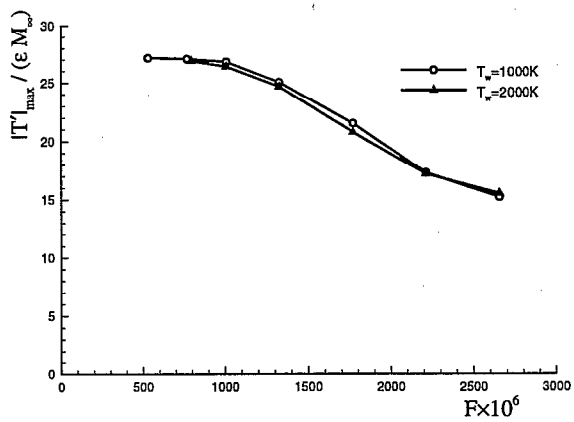

Figure 39: Distribution of receptivity coefficient $|A|$ vs. frequency for two cases of different wall temperatures at $\epsilon = 5 \times 10^{-4}$ ($T_w = 1000K$: Case A.1; $T_w = 2000K$: Case C.1).

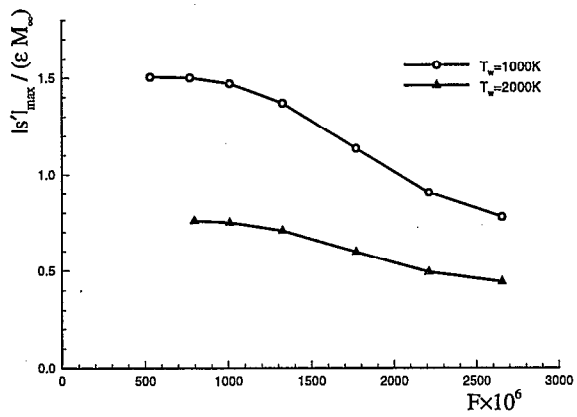

Figure 38: Distribution of receptivity coefficient $|A|$ vs. frequency for two cases of different wall temperatures at $\epsilon = 5 \times 10^{-4}$ ($T_w = 1000K$: Case A.1; $T_w = 2000K$: Case C.1).

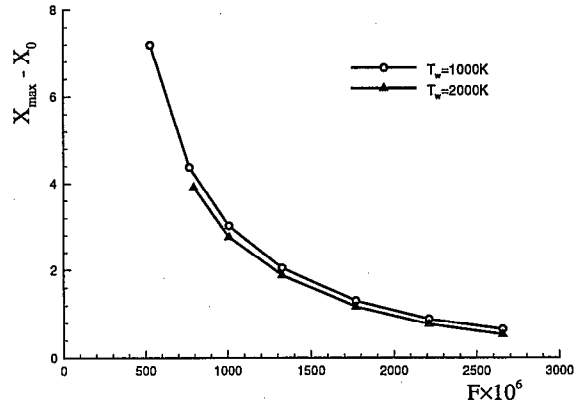

Figure 40: location of maximum entropy amplitudes vs. frequency for two cases of different wall temperatures at $\epsilon = 5 \times 10^{-4}$ ($T_w = 1000K$: Case A.1; $T_w = 2000K$: Case C.1).

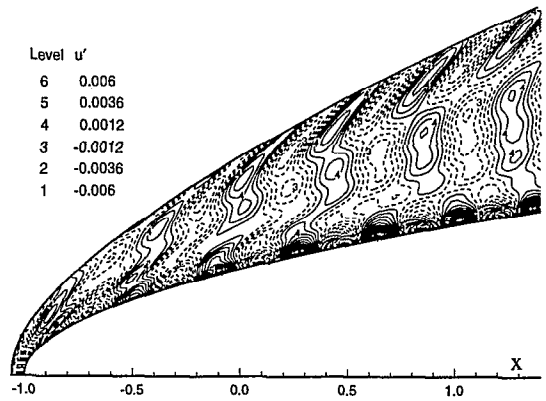

Figure 41: Contours of instantaneous perturbations of horizontal velocity components for Case D.2 of freestream acoustic waves at $F = 323$ and $Re_\infty = 60266$.

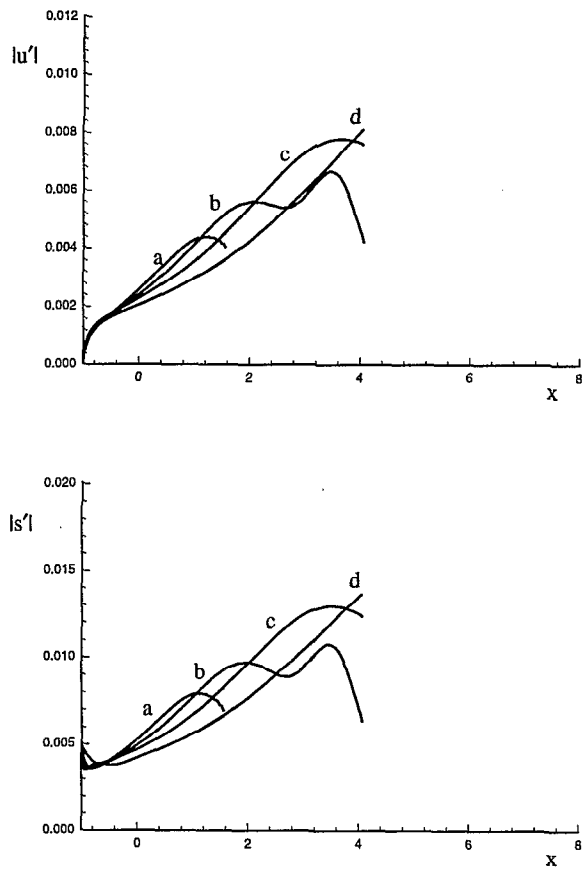

Figure 42: Variation of horizontal velocity and entropy perturbation amplitudes along the $i = 30$ grid line near the body surface with several forcing frequencies at $\epsilon = 5 \times 10^{-4}$ and $Re_\infty = 60266$ (Cases a to d in the figure correspond to Case D.2 to D.5 respectively).

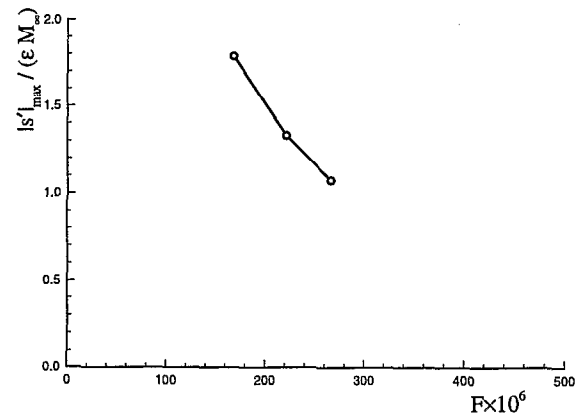

Figure 43: Distribution of receptivity coefficient $|A|$ vs. frequency for Cases D at $\epsilon = 5 \times 10^{-4}$ and $Re_\infty = 60266K$.